Peer Review Status Statement

This manuscript is a non-peer-reviewed preprint submitted to EarthArXiv.
This manuscript is currently under consideration at *International Journal of Applied Earth Observation and Geoinformation*.

Submitting author: Zezhi Yang
Submitting author's email address:yangzezhi24@mails.ucas.ac.cn
ORCID: https://orcid.org/0009-0007-3716-8586

Reconstructing annual 30 m forest aboveground biomass across Southwest China's karst region from 1986 to 2024

This manuscript is a preprint and has not been peer reviewed. It has been submitted to the International Journal of Applied Earth Observation and Geoinformation.

Zezhi Yang[1,2,3], Xiaoxin Zhang[4], Xiaowei Tong[1,2], Fuming Xie[5], Yuemin Yue[1,2], Kelin Wang[1,2], Martin Brandt[6]

[1]Huanjiang Observation and Research Station for Karst Ecosystem, Guangxi Key Laboratory of Karst Ecological Processes and Services, Institute of Subtropical Agriculture, Chinese Academy of Sciences, Changsha 410125, China.

[2]Institute of Subtropical Agriculture, Chinese Academy of Sciences, Changsha 410125, China.

[3]University of Chinese Academy of Sciences, Beijing 100049, China.

[4] Future Urbanity & Sustainable Environment (FUSE) Lab, Division of Landscape Architecture, Faculty of Architecture, The University of Hong Kong, Hong Kong SAR, China.

[5]School of Earth Sciences, Yunnan University, Kunming 650500, China.

[6]Department of Geosciences and Natural Resource Management, University of Copenhagen, Copenhagen, Denmark.

Correspondence: Xiaowei Tong (tongxiaowei@isa.ac.cn)

Abstract

Fine-resolution reconstruction of multi-decadal forest aboveground biomass (AGB) remains challenging in karst landscapes, where steep terrain, fragmented stands, and strong environmental gradients can limit the regional transferability of national and global products. We developed a regionally adapted two-stage framework to reconstruct annual 30 m forest AGB across Southwest China's karst region from 1986 to 2024 (KRAFT-30). First, National Forest Inventory (NFI) observations were integrated with Sentinel-2 imagery, canopy-height information, topography, and climate to construct a 2019 regional AGB baseline, with plot-level AGB allocated to 10 m pixels using an NDVI-weighted strategy. Second, the baseline was transferred to Landsat annual composites through biomass-stratified sampling, feature selection, four-model comparison, and XGBoost-based historical reconstruction, with uncertainty propagated across the two stages. The baseline agreed with withheld NFI plots ($R^2 = 0.75$; RMSE = 25.73 Mg ha^{-1}), and the selected Landsat model achieved $R^2 = 0.95$ and RMSE = 13.54 Mg ha^{-1} on the test set. More importantly, direct comparison with the existing national 30 m annual AGB product using the same NFI-6–NFI-9 references showed lower RMSE in all four inventory cycles and a lower regional mean bias (+16.6 versus +36.4 Mg ha^{-1}), while adjacent-period biomass changes agreed in direction with NFI observations in 81.2% of province–period combinations. Airborne LiDAR, GEDI, and independent vegetation indicators further supported structural and temporal consistency. The reconstructed series reveals substantial long-term biomass and aboveground-carbon accumulation while preserving fine-scale heterogeneity across fragmented karst forests. These results demonstrate the value of regional calibration and multi-source validation for long-term quantitative biomass monitoring in environmentally heterogeneous landscapes.

Keywords: Aboveground biomass; Landsat time series; Sentinel-2; Machine learning; Karst forests; Regional validation

1 Introduction

Forest aboveground biomass (AGB) is a fundamental variable for quantifying forest carbon stocks, tracking ecosystem recovery, and constraining land carbon-sink dynamics (Mitchard, 2018; Pan et al., 2011). Long, spatially explicit AGB records are particularly important where forest recovery and land-use transitions are rapid, because single-date maps cannot resolve the timing, magnitude, or spatial heterogeneity of biomass accumulation. In southern China, multi-decadal forest recovery and ecological restoration have generated strong demand for fine-resolution observations that can support regional carbon accounting and long-term forest monitoring (Lu et al., 2018; Tong et al., 2020, 2023).

Southwest China contains one of the world's largest contiguous karst regions, spanning Yunnan, Guizhou, Guangxi, and Hunan provinces (Wang et al., 2019). Steep terrain, shallow and discontinuous soils, strong hydrogeological contrasts, fragmented forest patches, and pronounced illumination and mixed-pixel effects create a particularly difficult setting for optical remote-sensing retrieval of forest biomass (Jiang et al., 2014; Lu et al., 2016; Wang et al., 2019). At the same time, extensive natural-forest protection, Grain-for-Green, and rocky-desertification control programs have altered forest structure and carbon storage over recent decades (Liu et al., 2008; Tong et al., 2018, 2023), making this region an important test bed for long-term quantitative biomass reconstruction.

Recent advances in optical, SAR, LiDAR, and machine-learning methods have produced increasingly detailed global and national AGB products (Dubayah et al., 2020; Santoro et al., 2021; Yang et al., 2023; Wang et al., 2025; Cai et al., 2025). In particular, national 30 m annual AGB mapping now provides multi-decadal coverage across China (Cai et al., 2025). The remaining challenge is therefore not simply data availability, but whether a uniform large-area model can preserve regional accuracy, local structural heterogeneity, and temporally coherent biomass change in highly fragmented karst forests. Regional transfer errors can arise from differences in forest structure, topography, environmental gradients, training-data representation, and optical saturation. A useful regional framework should consequently demonstrate measurable gains under common independent references rather than rely only on internal model fit or qualitative map comparisons.

Here, we developed a regionally adapted two-stage Sentinel-2–Landsat reconstruction framework for annual 30 m forest AGB during 1986–2024. The study has three linked objectives: (1) to construct a high-quality regional AGB baseline by integrating NFI observations with Sentinel-2, canopy-height, topographic, and climatic information, and to transfer this baseline to the Landsat archive using biomass-stratified sampling, feature selection, and model comparison; (2) to quantify regional performance through direct independent comparison with existing national and global AGB products using the same NFI references, complemented by airborne LiDAR, GEDI, uncertainty analysis, and temporal-consistency tests; and (3) to use the reconstructed annual series to characterize four decades of forest biomass and aboveground-carbon dynamics across karst and non-karst forests and among provinces. KRAFT-30 is retained as the name of the resulting annual map series, but the primary focus here is the reconstruction framework, its independently measured regional performance, and its long-term monitoring value.

2 Materials and methods

2.1 Study area

Southwest China contains one of the world's largest continuous karst regions, characterized by extensive carbonate-rock landscapes across Yunnan, Guizhou, Guangxi, and Hunan provinces (Fig. 1). The study area occupies a pivotal topographic transition zone extending from the southeastern margin of the Tibetan Plateau down to the low mountains and rolling hills of Southern China, covering 1.02 million km^2 totally (Fig. 1a, b). The region exhibits highly rugged terrain underlain by limestone and dolomite, forming a classic karst landscape with conical and tower-shaped hills, enclosed depressions, valleys, shallow and discontinuous soils, and strong hydrogeological heterogeneity (Jiang et al., 2014; Wang et al., 2019). Coupled with pronounced hydrogeological heterogeneity, these unique geomorphological attributes generate steep environmental gradients and highly fragmented forest patches, presenting a formidable challenge for remote-sensing-based biomass estimation (Lu et al., 2016; Wang et al., 2019).

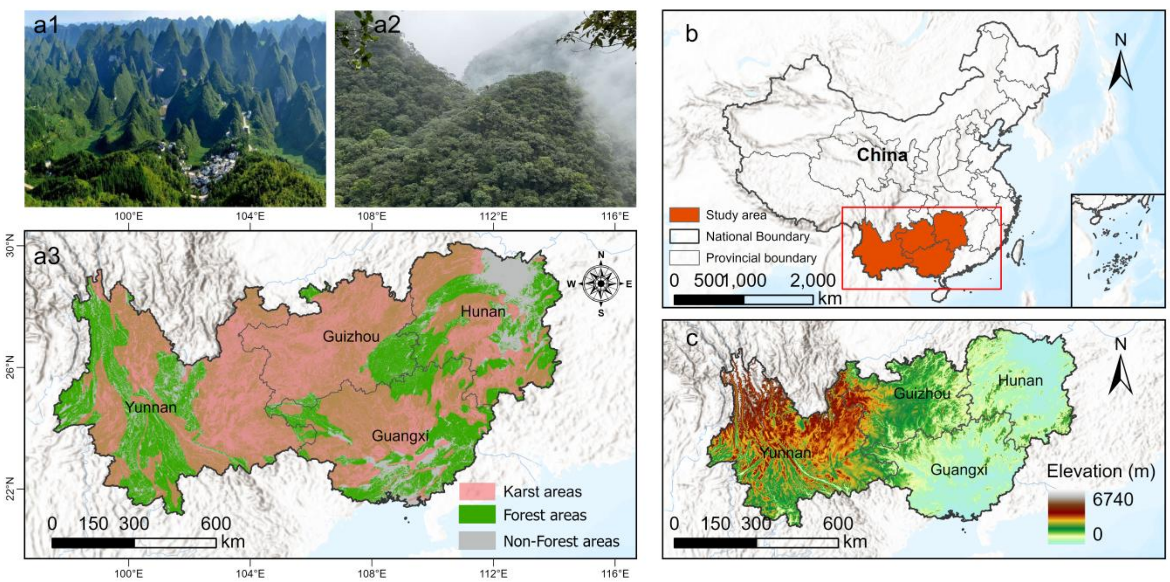

Figure 1. Overview of the Southwest China karst region. (a) Spatial distribution of forests and karst landforms in the study area. (b) Location of the study area in China. (c) Topographic characteristic of the karst landscape.

2.2 Data and reference datasets

The reconstruction and evaluation framework combined field inventory observations, Sentinel-2 and Landsat surface-reflectance data, canopy-height information, topographic and climatic covariates, land-cover masks, and independent structural and biomass reference products. Table 1 summarizes their roles in regional baseline mapping, historical reconstruction, independent comparison, and long-term analysis.

Table 1. Summary of datasets used for regional AGB reconstruction, validation, comparison, and analysis.

Purpose	Dataset	Spatial resolution	Temporal coverage	Quantity / extent	Reference
	Field survey data (NFI plot observations)	Plot-level	NFI-9 (2014-2018)	Plot observations for baseline modelling and validation	Zeng et al. (2015); Chinese NFI documentation / reports
Baseline map	Sentinel-2 Level-2A surface reflectance	10 m	2019 growing season	Study-area image composites	Drusch et al. (2012)
	ETH global canopy height product	10 m	Static covariate	Study-area canopy-height layer	Lang et al. (2023)
	SRTM DEM and terrain derivatives	30 m	Static covariate	Elevation, slope, and aspect	Farr et al. (2007)
	WorldClim bioclimatic variables	30 arc-sec (~1 km)	Long-term climatology	Bioclimatic covariates	Fick and Hijmans (2017)
Long-term map	Landsat surface reflectance annual composites	30 m	1986-2024	Annual cloud-reduced spectral composites	Wulder et al. (2019); USGS product documentation
	CLCD-derived semi-static forest mask	30 m	1990, 2005, and 2020	Stable forest-domain mask for 1986–2024 reconstruction	Yang and Huang (2021)
	Withheld NFI validation samples	Plot-level	Reference / validation period	893 withheld plots	Zeng et al. (2015); Chinese NFI documentation / reports
Validation and intercomparison	Multi-cycle NFI observations	Plot-level	NFI-6 to NFI-9 (1999-2018)	Four consecutive inventory cycles	Zeng et al. (2015); Chinese NFI documentation / reports
	Airborne LiDAR-derived canopy height model (CHM)	2 m	2017–2019	Coverage mainly across Guangxi	Data-source documentation
	GEDI L2A RH98 canopy-height observations	25 m footprint	2019–2022 and 2024	Footprint-level RH98 observations within the study area	Dubayah et al. (2021, 2020)
	Existing forest AGB products	30-100 m	Overlapping years	Yang map, Cai map, Su map, Wang map, and ESA CCI Biomass v6.0	Product-specific references
	Ecological indicators: GPP, NPP, LAI, SIF, and VOD	5km for GLASS GPP, NPP,LAI and GOSIF; 25km for VOD	Annual or growing-season annual composites over overlapping years	Regional annual mean time series	GLASS product documentation; Xiao et al.; Li and Xiao, 2019; Chen et al., 2025
Stratification and ancillary analysis	Karst distribution data	Vector	Static	Karst / non-karst stratification	Dataset documentation
	Provincial administrative boundaries	Vector	Static	Yunnan, Guizhou, Guangxi, and Hunan	Official data source
	Study-area boundary	Vector	Static	Analysis extent	Not applicable

Notes: AGB = aboveground biomass; CHM = Canopy Height Model; CLCD = China Land Cover Dataset; DEM = digital elevation model; NFI = National Forest Inventory; SRTM = Shuttle Radar Topography Mission.

2.2.1 NFI reference observations

National Forest Inventory (NFI) plot data from the sixth through ninth inventory cycles were used as the principal field reference (Zeng et al., 2015). After quality control, 3,637 valid permanent plots from the ninth cycle (NFI-9; 2014–2018) were retained across the study domain and adjacent reference provinces (Fig. 2). Plot-level AGB observations were quality controlled and co-registered with satellite-derived predictors (Chang et al., 2025). NFI-9 observations were divided into training and withheld validation subsets for regional baseline modelling and were also used as a common field reference for comparison with existing AGB products. Earlier NFI-6–NFI-8 observations, together with NFI-9, provided four consecutive inventory periods; 21,391 samples collected during 1999–2013 from the earlier cycles were used as temporally independent references for assessing the reconstructed time series and for direct comparison with the national annual AGB product. These inventories therefore support both contemporary spatial calibration and multi-period temporal evaluation.

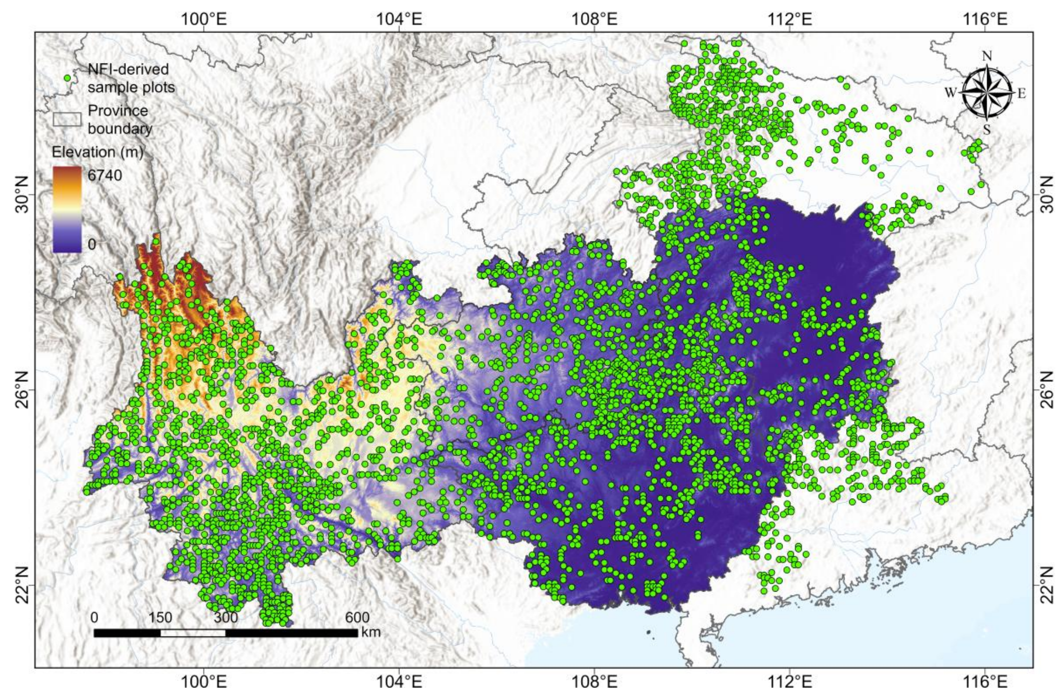

Figure 2. Location of the NFI-9 plots used in this study (n = 3637).

2.2.2 Satellite observations for AGB reconstruction

Sentinel-2 Level-2A imagery acquired during the 2019 growing season (May–October) was used to construct the regional baseline AGB map (Drusch et al., 2012). All harmonized Level-2A scenes with scene-level cloud cover below 40% were screened for clouds, cloud shadows, and dark pixels using Sentinel-2 cloud-probability information. Bands were resampled to a common 10 m grid, and a pixel-wise median composite was generated to derive spectral bands and vegetation indices. The combination of visible, red-edge, near-infrared, and shortwave-infrared information provides detailed sensitivity to canopy condition and helps characterize structural and compositional heterogeneity in mountainous forests (Puliti et al., 2021; Sibanda et al., 2015).

The Landsat archive was used for retrospective annual reconstruction from 1986 to 2024. Collection 2 Level-2 Tier-1 surface-reflectance imagery from Landsat 4/5 TM, Landsat 7 ETM+, and Landsat 8/9 OLI was obtained through Google Earth Engine at 30 m resolution (Masek et al., 2006; Vermote et al., 2016; Wulder et al., 2019). Cross-sensor spectral harmonization followed Roy et al. (2016), and clouds, cloud shadows, snow, and water were masked using quality-assessment flags. To improve spatiotemporal continuity and suppress residual noise, a forward three-year moving median was generated for each target year from 1986 to 2023 using observations from years t, t+1, and t+2; 2024 used the available forward two-year window. Each annual composite contained blue, green, red, NIR, SWIR1, and SWIR2 reflectance, together with NDVI and NBR. These eight variables formed the primary time-varying remote-sensing inputs to the historical AGB model.

2.2.3 Structural and environmental covariates

The regional baseline model used the ETH 10 m global canopy-height product (Lang et al., 2023), SRTM-derived elevation, slope, and aspect (Farr et al., 2007), and WorldClim bioclimatic variables representing annual mean temperature, temperature seasonality, and annual precipitation. The canopy-height layer supplied an explicit structural constraint for the 2019 baseline, while terrain and climate represented persistent environmental gradients that are pronounced across Southwest China's karst landscapes.

The China Land Cover Dataset (CLCD) was used to define the forest domain for annual reconstruction (Yang and Huang, 2021). To reduce sensitivity to year-specific classification noise and to maintain a consistent spatial support for long-term comparison, a semi-static forest mask retained pixels classified as forest in the representative years 1990, 2005, and 2020. This mask was applied consistently to the annual 30 m AGB maps from 1986 to 2024.

2.2.4 Independent validation, comparison, and stratification datasets

An airborne LiDAR-derived canopy height model (CHM) at 2 m resolution, acquired during 2017–2019 and covering most of Guangxi (~230,000 km²), was used as an independent structural reference. GEDI L2A Version 2 RH98 canopy-height observations for 2019–2022 and 2024 were quality filtered and spatially matched to the corresponding annual AGB estimates for complementary structural-consistency assessment (Dubayah et al., 2020; Earth Science Data Systems, 2025).

Publicly available AGB products covering the study area were assembled for direct comparison using common references and for spatial–temporal comparison. These included the 2019 China forest AGB map of Yang et al. (2023), the national 30 m annual AGB product of Cai et al. (2025; 1985–2023), static maps from Su et al. (2026) and Wang et al. (2025), ESA CCI Biomass v6.0 (Santoro et al., 2021; Santoro and Cartus, 2025), and the long-term radar-based product of Liu et al. (n.d.) for temporal comparison. Spatial extent, units, forest masks, and comparable years were harmonized according to the objective of each comparison.

Study-area, provincial, and karst-landform boundaries were used for regional summaries and stratified analyses. Temporal consistency was additionally evaluated against annual vegetation indicators representing canopy structure, productivity, and photosynthetic activity: GLASS GPP (Zheng et al., 2020), NPP (Yuan et al., 2010; Zheng et al., 2020), and LAI (Xiao et al., 2016), GOSIF v2 SIF (Li and Xiao, 2019), and the long-term C-band VOD record of Chen et al. (2025). Each product was clipped to the study area, restricted to the forest domain, and aggregated to annual regional means over its period of overlap with the reconstructed AGB series.

2.3 Regionally adapted two-stage AGB reconstruction framework

The framework was designed to combine the detailed regional calibration available from contemporary multi-source observations with the temporal depth of the Landsat archive (Fig. 3). Stage I generated a 2019 regional baseline using NFI observations, Sentinel-2 spectral information, canopy height, and environmental covariates. Stage II used the baseline as the AGB label source for biomass-stratified sampling and Landsat-based model development, followed by annual inference for 1986–2024. Independent comparison and validation were then used to test whether the regionalized reconstruction improved accuracy relative to existing products and preserved plausible structural and temporal behaviour.

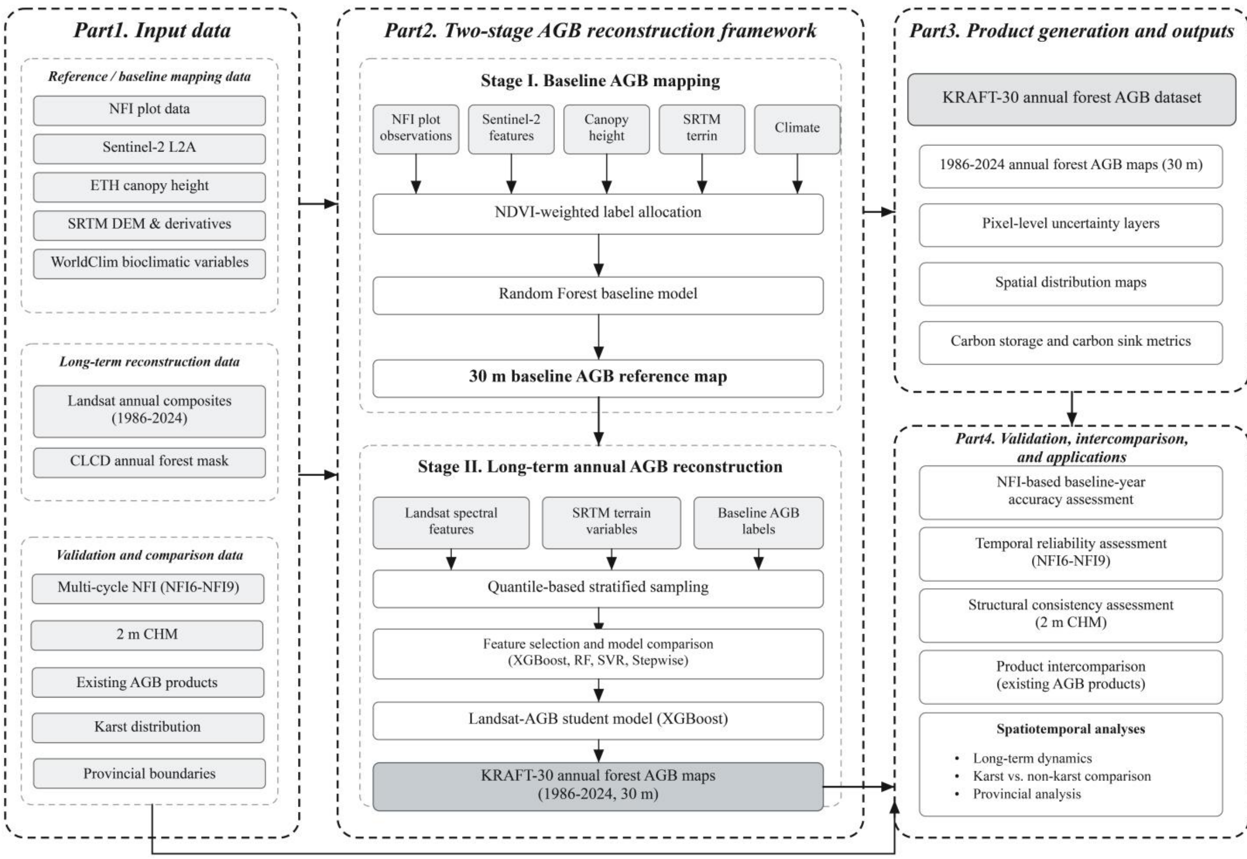

Figure 3. Regionally adapted two-stage framework for annual forest AGB reconstruction and independent evaluation.

2.3.1 Regional Sentinel-2 baseline AGB mapping

To generate a high-quality regional reference surface, NFI plot observations were integrated with Sentinel-2 imagery and environmental predictors. Because plot measurements and 10 m Sentinel-2 pixels have different spatial supports, plot-level AGB was allocated to 10 m pixels according to relative NDVI within each plot. Pixels with higher NDVI received proportionally larger shares of the observed plot AGB while preserving the plot total. The resulting NDVI-weighted 10 m labels provided spatially explicit response data aligned with the Sentinel-2 predictor grid.

Sixteen Sentinel-2 predictors were derived from the 2019 growing-season composite, including 10 multispectral bands and six vegetation indices (NDVI, EVI, SAVI, MSAVI2, NDMI, and NBR). Additional predictors included the ETH 10 m canopy height, SRTM elevation, slope and aspect, and the selected WorldClim bioclimatic variables (Table S1). A random forest model was trained using the NDVI-weighted

AGB labels and applied across the study area to generate a 10 m baseline map, which was subsequently aggregated/aligned to support the 30 m Landsat reconstruction stage.

2.3.2 Landsat-based annual AGB reconstruction

2.3.2.1 Biomass-stratified sampling of baseline labels

Because low-to-moderate biomass dominates much of the karst region, a hybrid stratified sampling strategy was used to prevent the training pool from being overwhelmed by low-value pixels while retaining rare high-biomass conditions. For baseline AGB values of 0–300 Mg ha^{-1}, six equal-frequency strata were defined by AGB quantiles (McKay et al., 1979), and 15,000–40,000 samples were selected per stratum to limit redundancy. All 13,648 pixels with AGB ≥ 300 Mg ha^{-1} were retained. The resulting samples were randomly divided into training (80%) and test (20%) subsets using a fixed random seed.

2.3.2.2 Model comparison, feature selection, and historical inference

The 2019 baseline AGB estimates were used as response labels, while Landsat-derived spectral variables and SRTM-derived terrain variables were used as predictors (Table S2). Four algorithms were evaluated: XGBoost (Chen and Guestrin, 2016), random forest (Breiman, 2001), support vector regression (Drucker et al., 1997), and stepwise regression (Efroymson, 1960). Key hyperparameters were optimized by grid search with five-fold cross-validation, and final models were fitted using the optimal settings.

Predictor redundancy was reduced through sequential feature addition based on XGBoost gain importance. The top n variables (n = 10, 15, 20, …, 51) were added in increments of five, and the optimal feature set was selected from test-set R^2 and RMSE (Fig. S2). The best-performing algorithm and feature subset were then applied to each annual Landsat composite to reconstruct forest AGB for 1986–2024. SHAP analysis was used to quantify predictor contributions and the direction of feature effects (Lundberg and Lee, 2017).

2.3.3 Pixel-level uncertainty quantification

Pixel-level uncertainty was estimated separately for the regional baseline and the Landsat reconstruction stages and combined by Gaussian error propagation (Ku, 1966). Baseline uncertainty was derived from RMSE calculated within intervals of predicted AGB using withheld NFI samples and assigned spatially according to the corresponding biomass range, producing a baseline uncertainty layer σ_1. Reconstruction uncertainty was estimated using an XGBoost absolute-residual model driven by the same spectral and terrain features as the AGB model, with predicted AGB included as an additional predictor, producing annual reconstruction uncertainty σ_2. Assuming independence between the two components, total annual uncertainty was calculated as:

$$\sigma_{total} = \sqrt{\sigma_1^2 + \sigma_2^2}$$

where σ denotes the total annual uncertainty, σ_1 and σ_2 represent baseline and reconstruction uncertainties, respectively. All uncertainty estimates are expressed in Mg ha^{-1}.

2.4 Independent validation and comparison with existing AGB products

The baseline map and reconstructed AGB estimates were evaluated against withheld NFI observations using the coefficient of determination (R^2), root mean square error (RMSE), mean absolute error (MAE), and systematic bias (Bias). These metrics quantify explained variation, error magnitude, and systematic over- or underestimation and were calculated as follows:

$$R^2 = 1 - \frac{\sum_{i=1}^{n} (P_i - O_i)^2}{\sum_{i=1}^{n} (O_i - \bar{O})^2} \tag{1}$$

$$RMSE = \sqrt{\frac{1}{n}\sum_{i=1}^{n}(P_i - O_i)^2} \tag{2}$$

$$MAE = \frac{1}{n}\sum_{i=1}^{n}|P_i - O_i| \tag{3}$$

$$Bias = \frac{1}{n}\sum_{i=1}^{n}(P_i - O_i) \tag{4}$$

where O_i and P_i are observed and predicted AGB of the ith validation sample, respectively, $\bar{O}$ is mean observed AGB, and n is the number of validations.

2.4.1 NFI-based comparison with the national annual AGB product

A central test was conducted against the national 30 m annual AGB product of Cai et al. (2025) using the same multi-cycle NFI observations, temporal matching rules, and spatial extraction procedures. For each NFI-6–NFI-9 period, plot-scale Pearson correlation, RMSE, MAE, and Bias were calculated for both products. Prediction–observation scatterplots were used to compare accuracy and systematic error across consecutive inventory cycles.

At the regional scale, inventory-period mean AGB was summarized for NFI observations, the regional reconstruction, and the Cai product across the full study area and within Yunnan, Guizhou, Guangxi, and Hunan. Bias relative to the NFI mean was used to assess regional temporal consistency. Changes between adjacent inventory periods were further compared using province × inventory interval as the evaluation unit, and directional agreement, change bias, MAE, RMSE, linear slope, and correlation were summarized (Table S3).

2.4.2 Common-reference comparison across biomass gradients and spatial structure

Existing AGB products were compared after harmonizing spatial extent, units, forest masks, and comparable years. For the common NFI-9 comparison, product estimates were evaluated against the same 893 withheld NFI samples, and residuals were summarized along observed AGB gradients to test low-, moderate-, and high-biomass behaviour. Spatial detail was examined in representative regions of interest, while time-series products were compared through regional annual mean trajectories over overlapping years.

Forest masks were selected according to comparison objective. Time-series comparisons used the 30 m semi-static CLCD forest mask; for coarser products, forest fraction was aggregated to the native grid and cells with ≥70% forest cover were retained. CHM-based comparisons used a 2019 tree-probability mask with a 50% threshold, while original masks were retained for the Yang and Cai products. The 2 m CHM was averaged and aligned to each product grid before structural comparison.

2.5 Additional structural and temporal reliability assessment

2.5.1 Airborne LiDAR and GEDI structural consistency

Structural consistency was assessed using the airborne LiDAR CHM. Because canopy height and AGB are nonlinearly related, ln(CHM) was used as the structural reference and Pearson correlation was calculated between each AGB product and the corresponding log-transformed canopy height.

$$r = \frac{\sum_{i=1}^{n} (A_i - \bar{A})(C_i - \bar{C})}{\sqrt{\sum_{i=1}^{n} (A_i - \bar{A})^2}\sqrt{\sum_{i=1}^{n} (C_i - \bar{C})^2}} \tag{5}$$

where A_i denotes the KRAFT-30 AGB value of the ith spatial unit, C_i denotes the corresponding ln(CHM) value, and $\bar{A}$ and $\bar{C}$ are the respective means. This analysis was used to evaluate the spatial plausibility of KRAFT-30 from the perspective of canopy-structure gradients.

2.5.2 Cross-product and ecological temporal consistency

For temporal corroboration beyond NFI inventories, regional annual mean AGB was compared with the long-term products of Cai et al. and Liu et al. over overlapping years. Pearson correlations were also calculated between the reconstructed AGB trajectory and independent annual VOD, GPP, NPP, LAI, and SIF series. These comparisons were treated as temporal-consistency evidence rather than direct plot-level AGB validation.

2.6 Long-term biomass and aboveground-carbon dynamics

The annual 1986–2024 reconstruction was used to characterize long-term biomass dynamics at pixel, geomorphological, provincial, and regional scales. The Theil–Sen slope was calculated for each forest pixel to quantify the direction and magnitude of long-term AGB change:

$$Slope = median\left(\frac{AGB_j - AGB_i}{j - i}\right), \quad 1986 \leq i < j \leq 2024 \tag{6}$$

where AGB_i and AGB_j are the AGB values of the same pixel in years i and j, respectively. The slope represents the annual rate of AGB change and is expressed in Mg $ha^{-1}yr^{-1}$. The Theil-Sen slope is robust to outliers and is widely used to estimate long-term trends (Sen, 1968). Annual mean AGB was also calculated for the entire study area, karst and non-karst regions, and the four provinces of Yunnan, Guizhou, Guangxi, and Hunan to compare forest AGB dynamic in forest AGB across different geomorphological settings and administrative regions.

To quantify regional aboveground carbon-stock dynamics, the annual AGB maps were checked for NoData values, grid consistency, and spatial alignment. Pixel areas were calculated from the grid resolution with correction for latitudinal variation. Total aboveground forest biomass in each year was calculated as:

$$B_t = \sum_{i=1}^{n_t} AGB_{i,t} \times S_i \tag{7}$$

where B_t is total forest biomass in year t, with units of Mg; $AGB_{i,t}$ is the AGB density of the ith valid forest pixel in year t, with units of Mg ha^{-1}; S_i is the pixel area, with units of ha; and n_t is the number of valid forest pixels in year t.

Annual forest carbon stock was estimated using a biomass-to-carbon conversion factor of 0.47:

$$C_t = \frac{B_t \times f_C}{10^6}, \quad f_C = 0.47 \tag{8}$$

where C_t is forest carbon stock in year t, with units of Tg C; f_C is the carbon conversion coefficient. Annual net carbon change was calculated as the difference in carbon stock between adjacent years:

$$\Delta C_t = C_t - C_{t-1} \tag{9}$$

where ΔC_t is the change in aboveground forest carbon stock from year t-1 to year t, with units of Tg C/yr. Finally, long-term trends in aboveground carbon stock and mean carbon-stock accumulation per unit forest area were calculated to characterize regional carbon accumulation.

3 Results

3.1 Performance of the two-stage AGB reconstruction framework

3.1.1 Regional Sentinel-2 baseline performance

The regional baseline model was driven jointly by canopy structure, environmental gradients, and Sentinel-2 spectral information (Fig. 4). Canopy height was the most important individual predictor, followed by temperature seasonality, elevation, annual mean temperature, and key Sentinel-2 bands. At the feature-group level, Sentinel-2 spectral and vegetation variables contributed 58.2%, terrain and canopy-height information 22.5%, and climate variables 19.3%, indicating that the baseline combined complementary structural, spectral, and environmental constraints across the heterogeneous karst landscape.

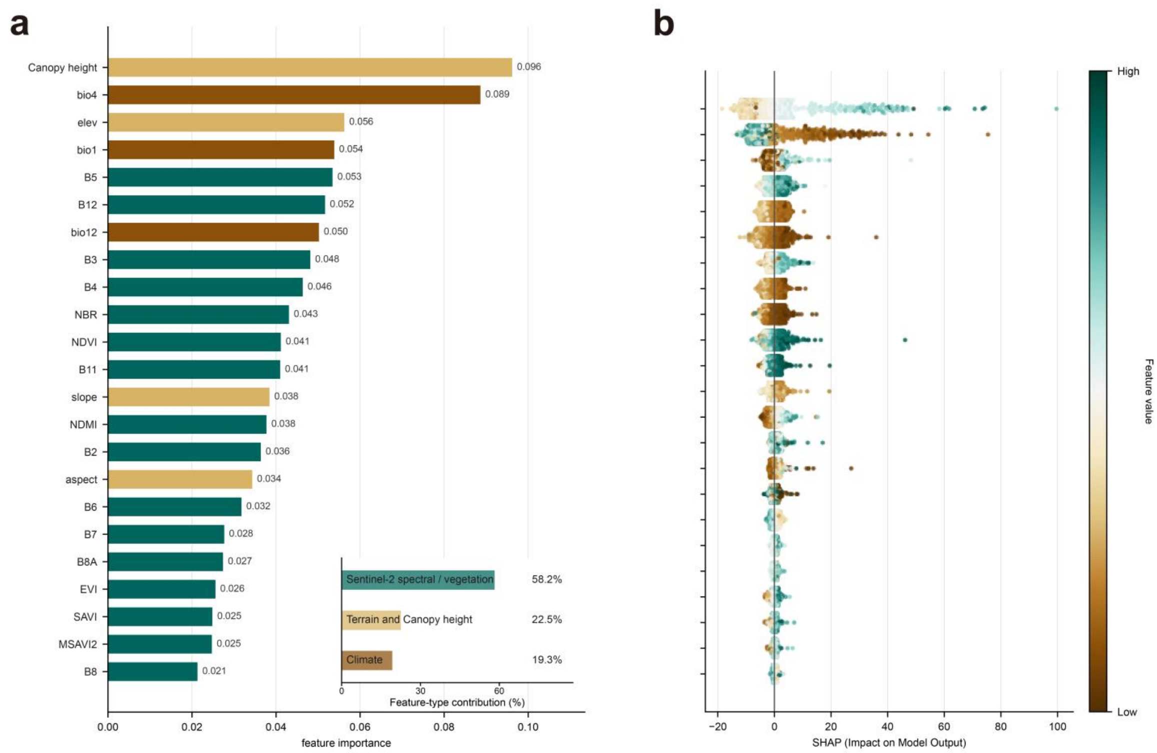

Figure 4. Feature Importance for the baseline AGB map. (a) Ranking of feature importance. (b) SHAP impact values of AGB baseline model features on estimated AGB values.

Against withheld NFI observations, the baseline map achieved $R^2 = 0.75$, RMSE = 25.73 Mg ha^{-1}, MAE = 12.01 Mg ha^{-1}, and Bias = −3.42 Mg ha^{-1} (Fig. 5a). Agreement was strongest below approximately 200 Mg ha^{-1}. The predicted and observed distributions were both right-skewed and concentrated mainly within 50–150 Mg ha^{-1}, although the model compressed part of the upper biomass range (Fig. 5b).

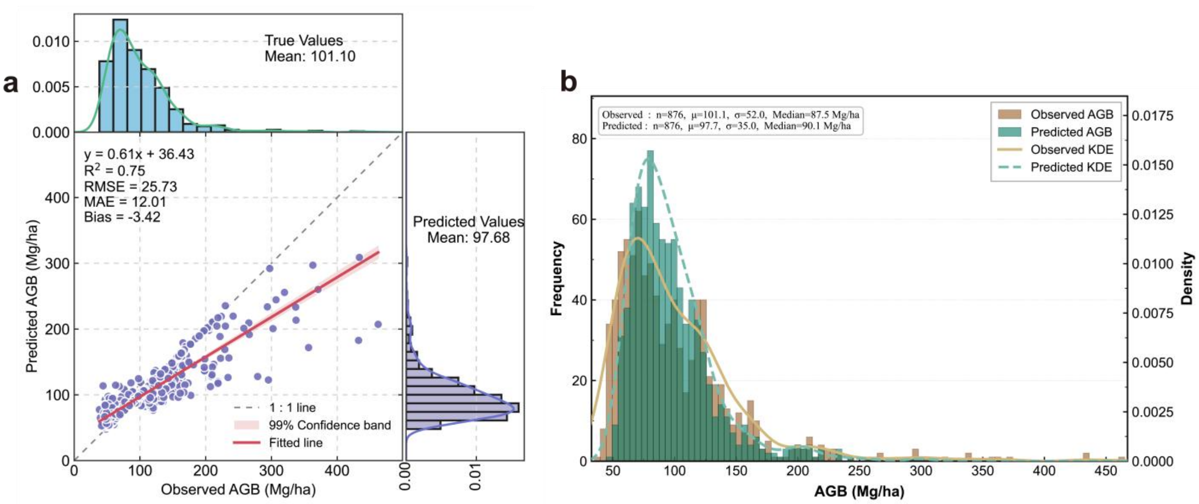

Figure 5. Accuracy assessment of the baseline AGB model. (a) Scatterplot of predicted AGB and NFI-observed AGB (n = 893). (b) Frequency distributions of predicted and NFI-observed AGB. KDE is kernel density estimate.

3.1.2 Landsat-based annual reconstruction and model selection

The 2019 regional baseline was used as the response-label source for Landsat-based model development and annual reconstruction for 1986–2024.

All four candidate algorithms produced positive predictive skill, but XGBoost clearly performed best (R^2 = 0.95, RMSE = 13.54 Mg ha^{-1}, MAE = 8.53 Mg ha^{-1}, Bias = −0.06 Mg ha^{-1}) and was selected for final reconstruction (Fig. 6). SHAP analysis showed that Landsat spectral bands and vegetation indices contributed most strongly, with terrain variables providing secondary constraints; individual predictors exhibited distinct positive and negative effects on model output (Fig. 7).

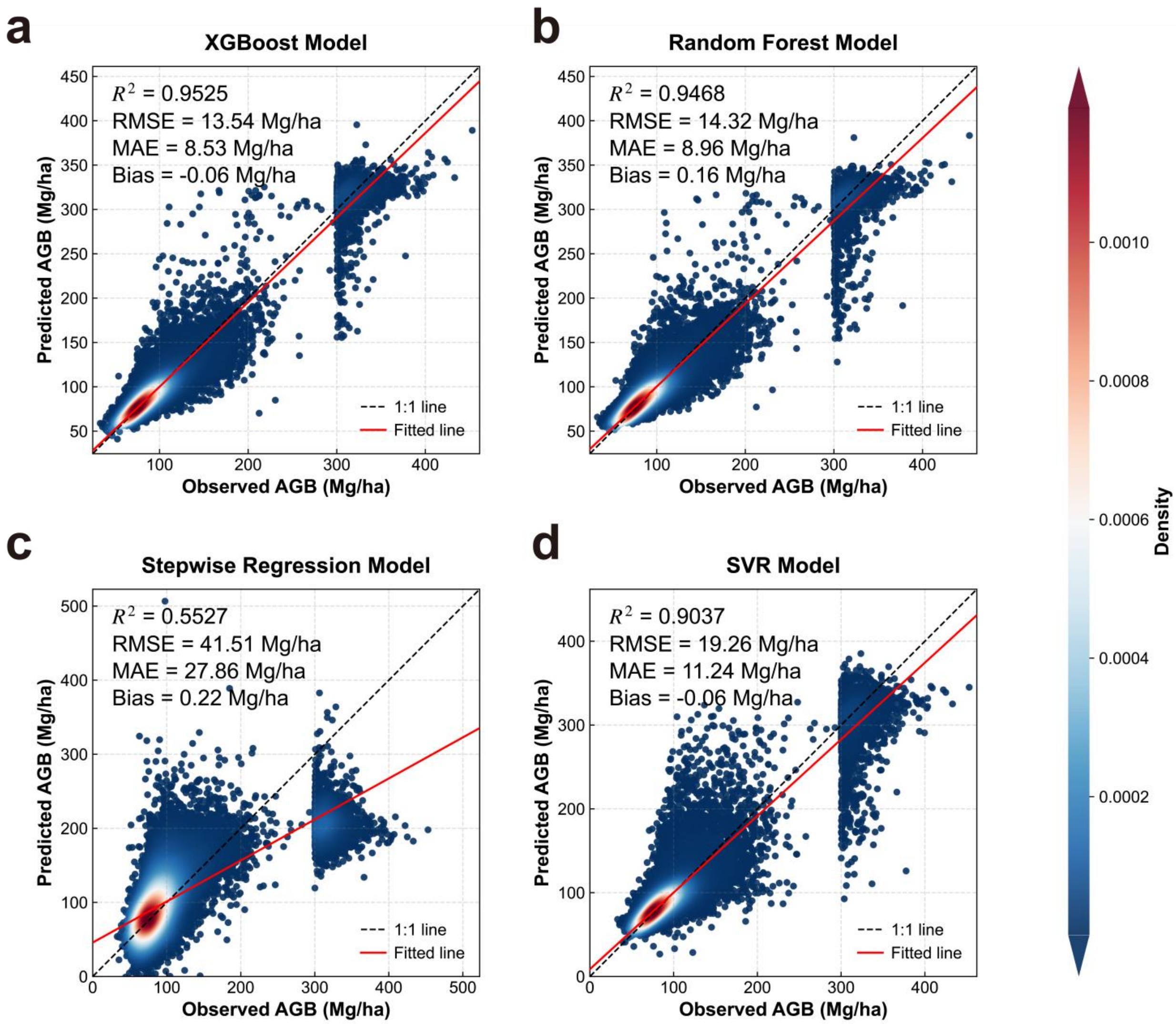

Figure 6. Performance comparison of Landsat-based AGB reconstruction models using different algorithms. (a)–(d) Comparisons between predicted and observed AGB for the XGBoost, Random Forest (RF), Stepwise Regression, and Support Vector Regression (SVR) models, respectively. The black dashed line indicates the 1:1 line, and the red solid line indicates the fitted regression line.

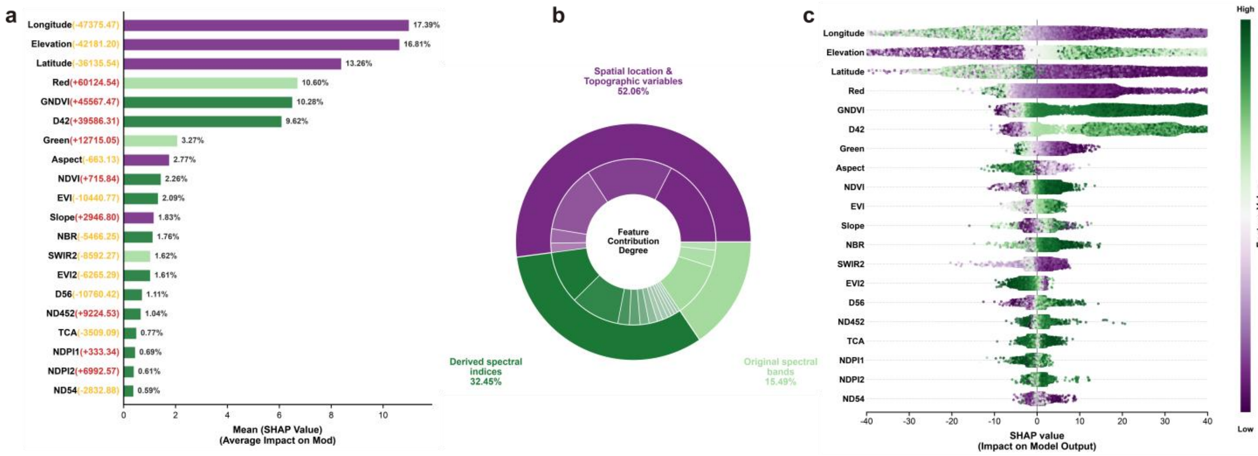

Figure 7. SHAP-based interpretation of feature importance and effects in the Landsat-based AGB reconstruction model. (a) Ranking of the top predictors according to their mean absolute SHAP values. (b) Relative contributions of different predictor groups, including spatial location and topographic variables, derived spectral indices, and original spectral bands. (c) SHAP summary plot showing the direction and magnitude of each predictor's effect on AGB predictions, where each point represents one sample and the colour indicates the corresponding feature value. SHAP denotes Shapley additive explanations.

3.2 Independent comparison with existing AGB products

We prioritized comparisons using common independent references to determine whether regional adaptation produced measurable gains beyond existing large-area AGB products. The strongest evidence came from consecutive NFI inventories, a common withheld NFI comparison across biomass gradients, and fine-scale spatial comparison in fragmented karst forests.

3.2.1 Multi-cycle NFI comparison with the national annual AGB product

Across four consecutive NFI inventory periods, the regional reconstruction maintained stable positive agreement with NFI-observed AGB and lower error than the national annual product of Cai et al. under the same field reference (Fig. 8A). Correlations for the regional reconstruction were 0.58, 0.56, 0.57, and 0.57 from NFI-6 to NFI-9. Corresponding RMSE values were 56.6, 64.2, 65.5, and 42.1 Mg ha^{-1}, compared with 85.8, 76.5, 81.1, and 69.6 Mg ha^{-1} for the Cai product; MAE values were likewise lower in all four periods. In NFI-9, Bias was close to zero (−3.0 Mg ha^{-1}).

The same advantage was evident at regional scale (Fig. 8B). Across 1999–2018, the reconstructed means tracked the multi-period NFI trajectory more closely, with a full-region mean Bias of +16.6 Mg ha^{-1} versus +36.4 Mg ha^{-1} for the Cai product. Provincial comparisons showed a similar pattern, while adjacent-period changes matched the direction of NFI-observed change in 81.2% of province–inventory-period combinations (Table S3).

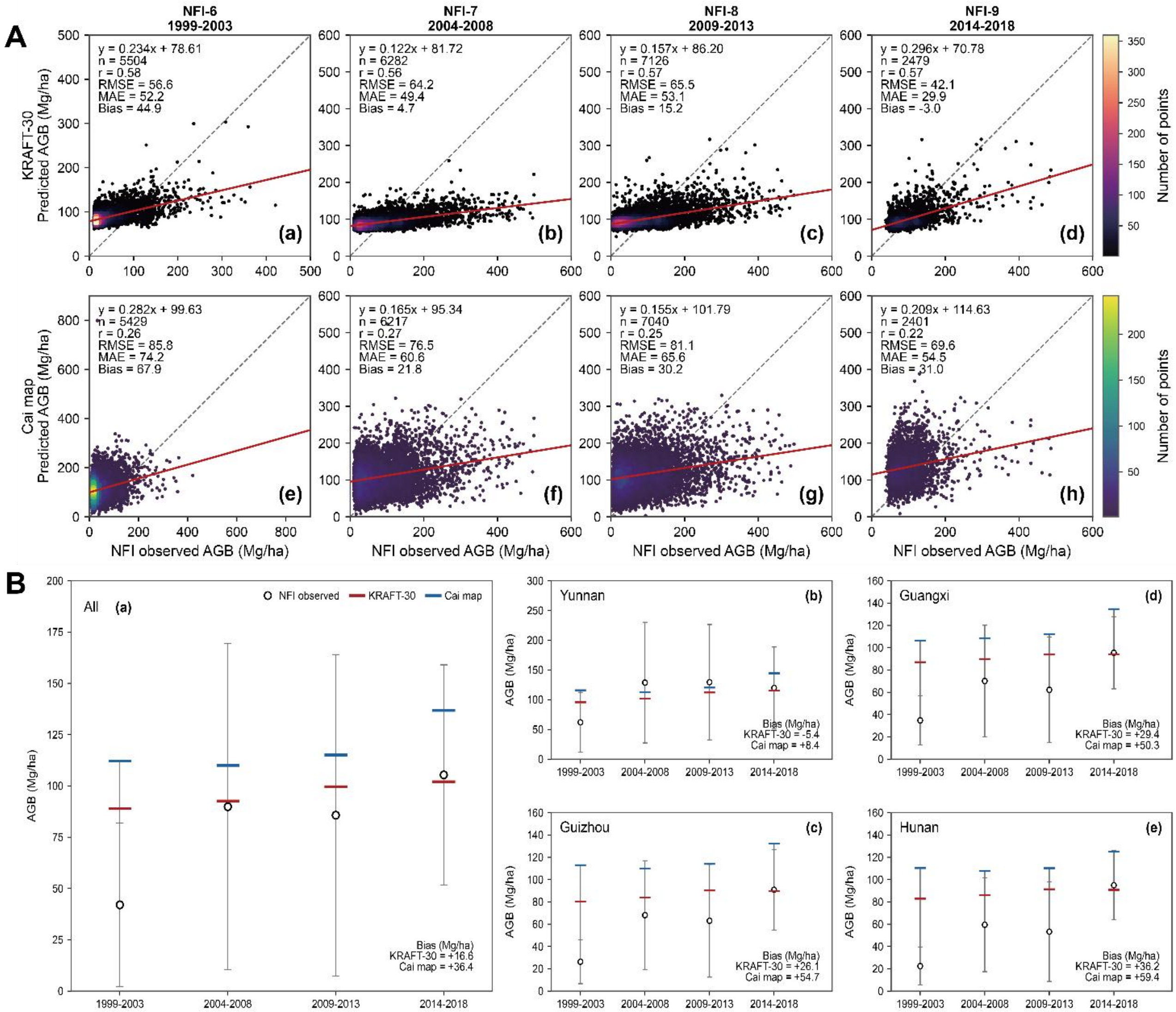

Figure 8. Multi-cycle NFI comparison of the regional reconstruction and Cai et al.'s national annual AGB product. (A) Plot-scale accuracy across NFI-6–NFI-9. (B) Regional mean consistency across four inventory phases.

3.2.2 Comparison across AGB gradients using common NFI samples

Using the same 893 withheld NFI samples, we compared the regional reconstruction with five existing AGB products under a common NFI reference: Yang et al. (2023), Cai et al. (2025), Su et al. (2026), Wang et al. (2025), and ESA CCI Biomass v6.0 (Santoro et al., 2021). The regional reconstruction had the lowest RMSE, MAE, and absolute Bias among the evaluated products (Fig. 9A). Residuals were generally centred near zero at low-to-moderate biomass. Above 250 Mg ha^{-1}, all optical/multi-source products showed increasing negative residuals, but the regional reconstruction exhibited comparatively smaller underestimation, indicating a weaker high-biomass compression under the same field reference (Fig. 9B).

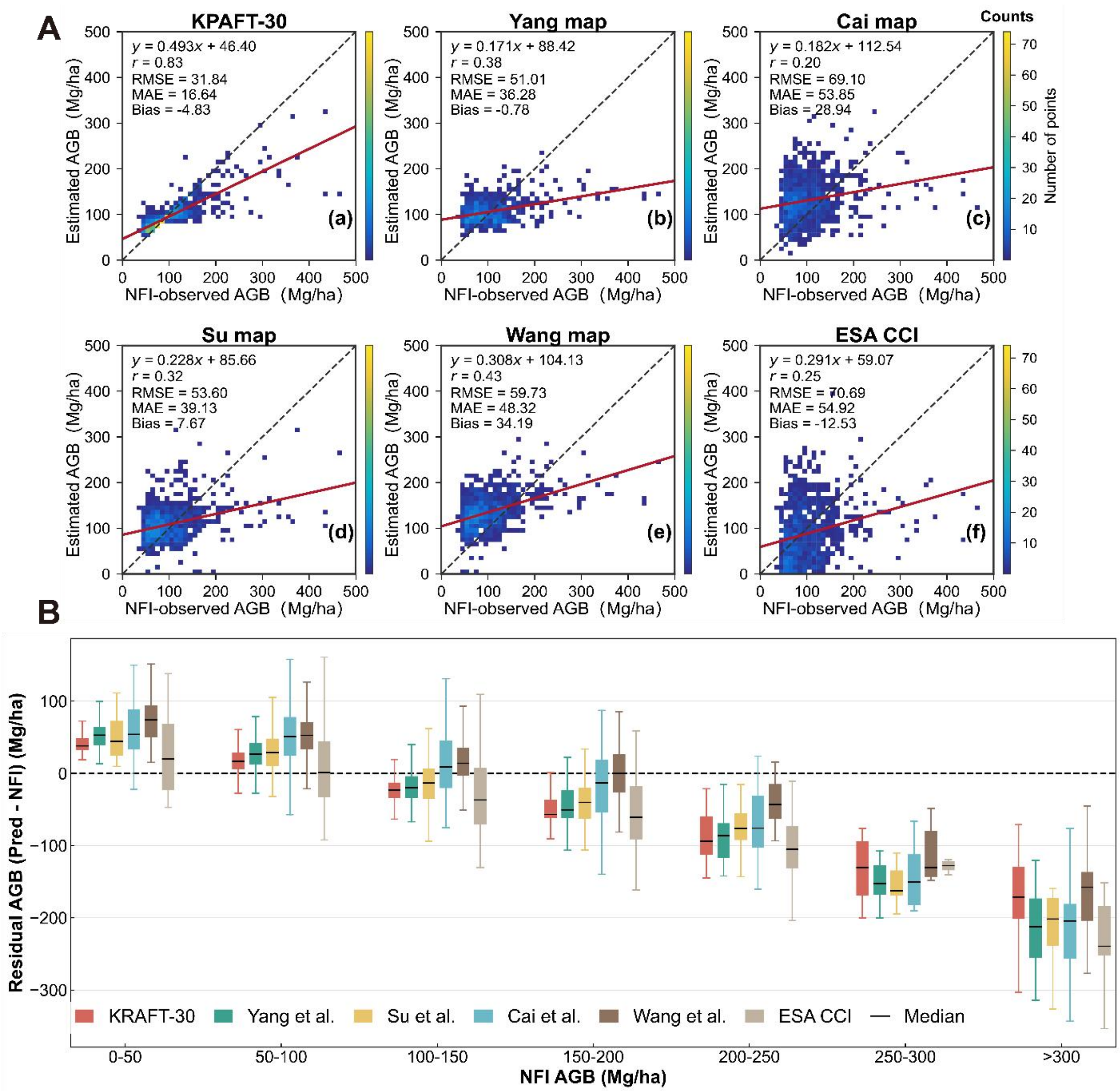

Figure 9. Common-NFI evaluation and residual comparison of the regional reconstruction and existing forest AGB products. (A) Product-estimated versus NFI-observed AGB for KRAFT-30, Yang, Cai, Su, Wang, and ESA CCI Biomass v6.0. (B) Residual distributions along NFI-observed AGB gradients. All comparisons use the same 893 withheld NFI samples.

3.2.3 Fine-scale spatial information in fragmented karst forests

Fine-scale comparison in representative regions of interest showed that the regional reconstruction retained greater spatial heterogeneity in fragmented mountain forests than the coarser or more spatially smoothed comparison products (Fig. 10). Forest edges, small patches, transition zones, and within-landscape biomass gradients remained visible at 30 m, while high-biomass areas preserved coherent spatial structure without the strong blockiness or smoothing apparent in several alternatives. Together with the common-NFI residual analysis, these patterns support a regional advantage in representing heterogeneous karst forest structure rather than merely increasing nominal spatial resolution.

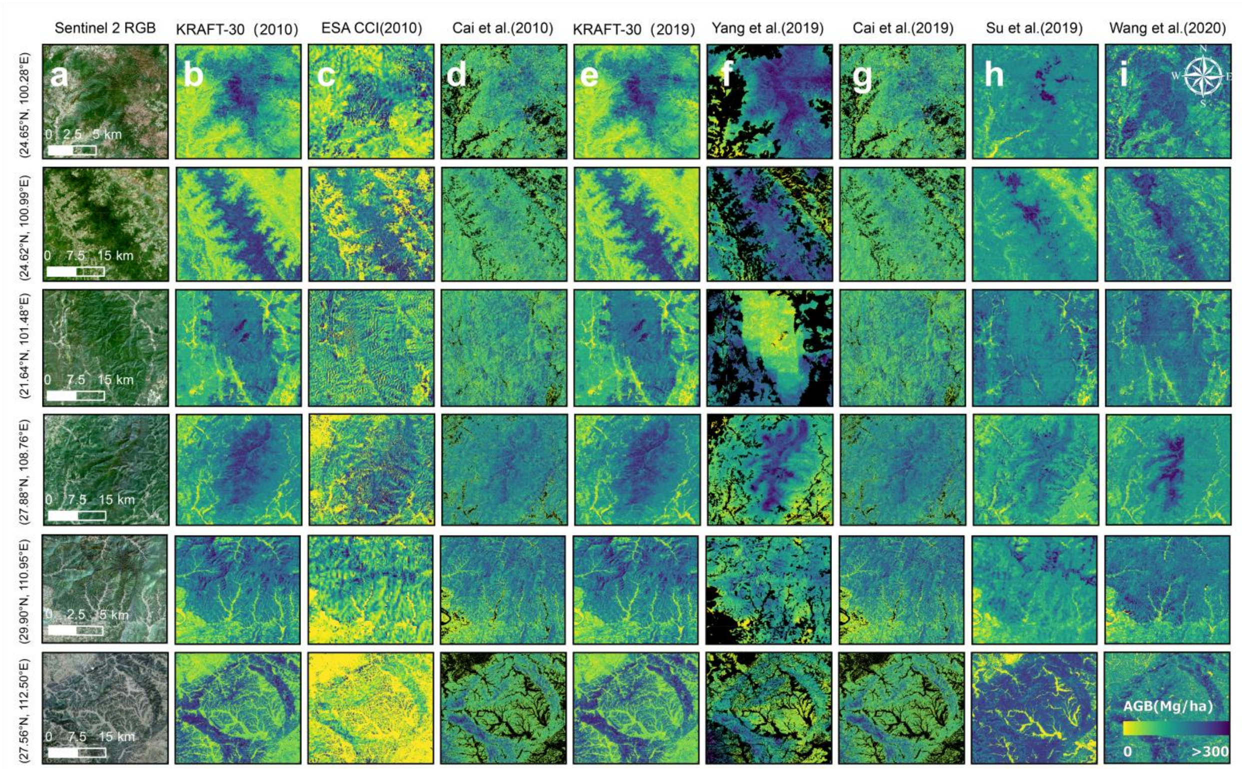

Figure 10. Fine-scale spatial comparison of the regional reconstruction with existing forest AGB products. (a) Sentinel-2 RGB imagery for representative regions of interest. (b)–(d) AGB maps for 2010 from KRAFT-30, ESA CCI Biomass, and Cai et al.; (e)–(i) 2019 AGB maps from KRAFT-30, Yang et al., Cai et al., Su et al., and Wang et al.

3.3 Additional structural and temporal reliability assessment

3.3.1 Structural consistency with airborne LiDAR and GEDI

The regional reconstruction showed a significant positive relationship with log-transformed airborne LiDAR canopy height ($r = 0.301$, $p < 0.001$) and the highest CHM correlation among the products evaluated in this structural comparison (Fig. 11). The absolute correlation was modest, as expected for a canopy-height proxy rather than direct AGB measurements, but the relative result indicates improved correspondence with independent vertical-structure gradients.

Across all years with GEDI observations (2019–2022 and 2024), annual AGB estimates retained significant, temporally stable positive relationships with GEDI RH98 (Fig. 12), providing an additional independent check that the reconstructed maps preserved spatial correspondence with spaceborne canopy structure.

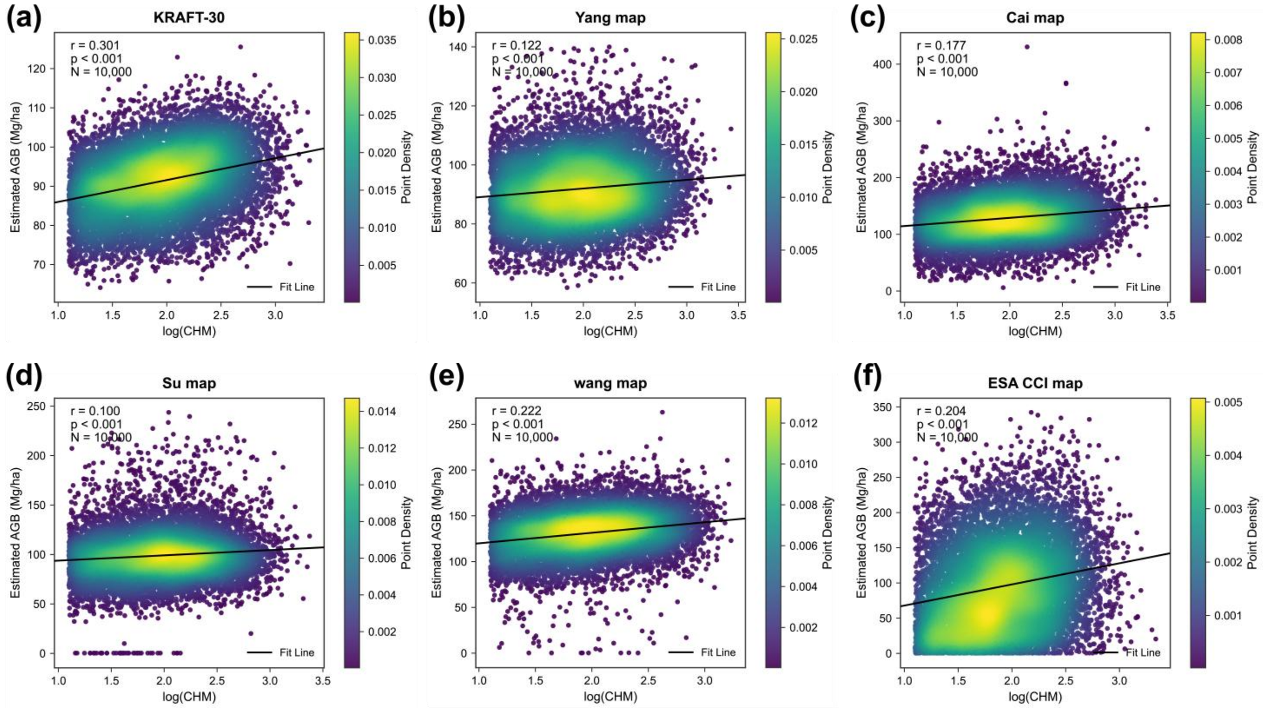

Figure 11. Structural consistency with airborne LiDAR canopy height. (a) Relationship between KRAFT-30 AGB and log-transformed CHM. (b)–(f) Corresponding relationships for Yang, Cai, Su, Wang, and ESA CCI Biomass. The black line denotes the fitted relationship.

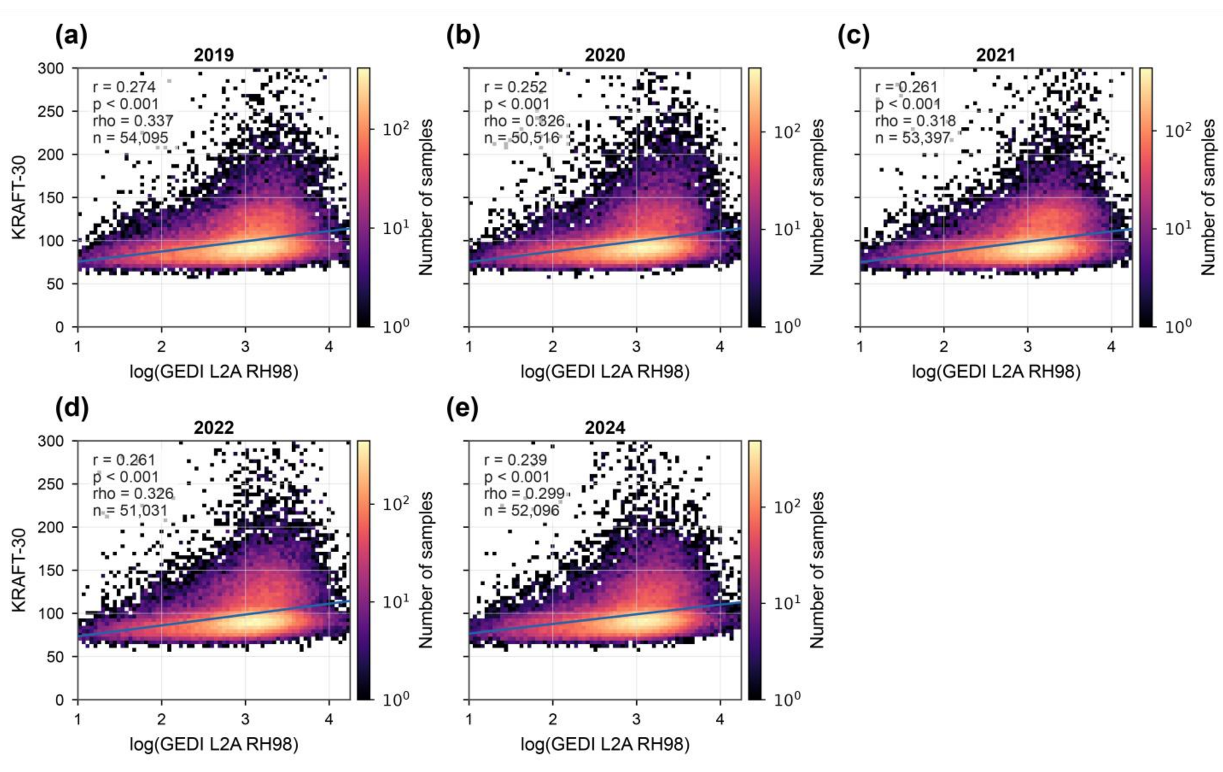

Figure 12. Structural consistency of annual AGB estimates with GEDI L2A RH98 canopy height for 2019, 2020, 2021, 2022, and 2024. Colours denote sample density and the fitted line summarizes the spatial relationship in each year.

3.3.2 Pixel-level uncertainty characteristics

Pixel-level uncertainty was concentrated mainly between 25 and 55 Mg ha^{-1} (Fig. 13a). Higher uncertainty occurred primarily in high-biomass mountainous forests, particularly western Yunnan and parts of Guangxi and Hunan, whereas lower-biomass areas such as Guizhou generally showed smaller values. Regional mean uncertainty remained within a relatively narrow range of approximately 33–40 Mg ha^{-1} over 1986–2024, with only modest long-term variation (Fig. 13b,c).

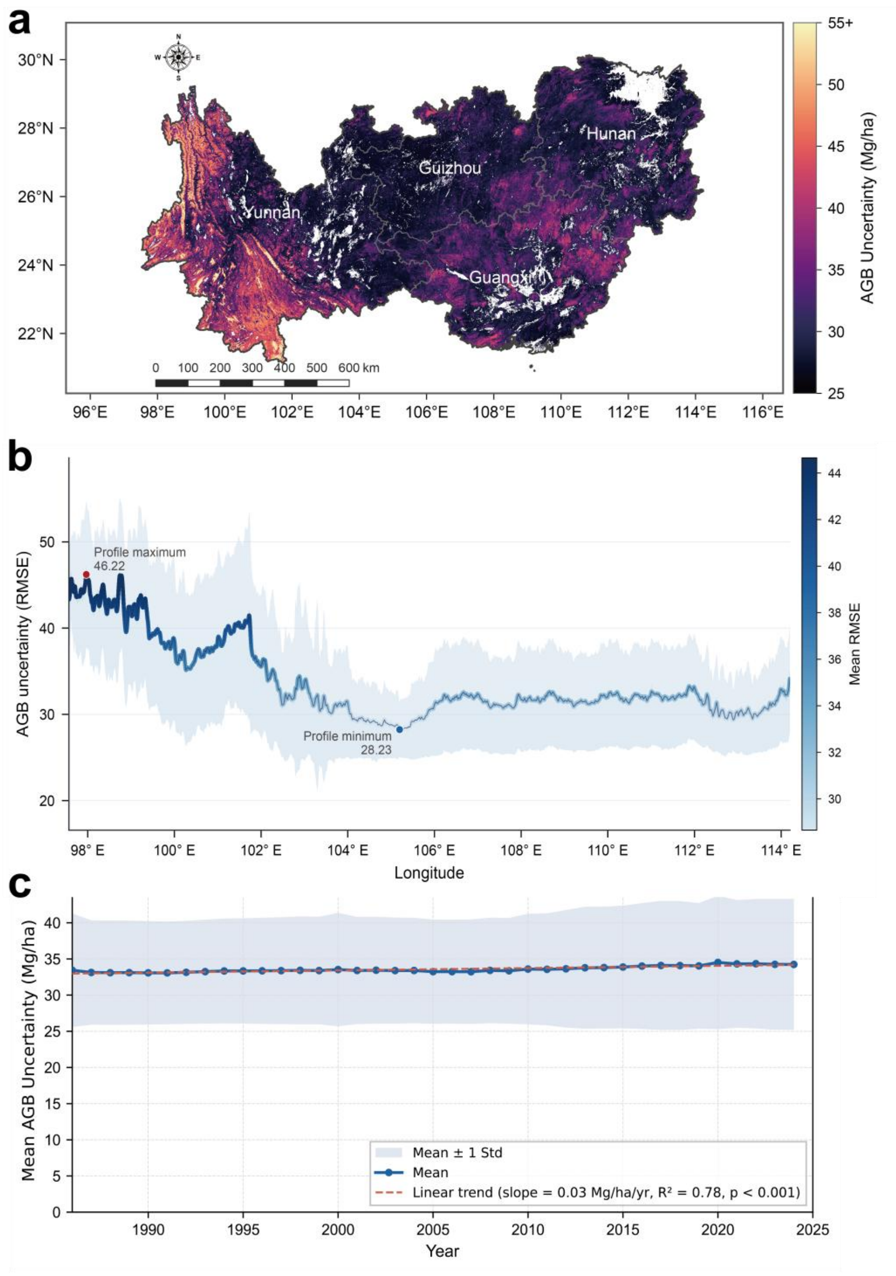

Figure 13. Spatial and temporal patterns of pixel-level uncertainty in annual forest AGB estimates during 1986–2024. (a) Mean uncertainty. (b) Longitudinal profile of mean uncertainty. (c) Annual regional mean uncertainty.

3.3.3 Cross-product and ecological temporal consistency

The reconstructed regional mean trajectory was strongly correlated with the two independent long-term AGB products over their overlapping periods (Fig. 14; Table 2). Pearson r was 0.96 against Cai et al. for 1986–2023 and 0.87 against Liu et al. for 1993–2020 (both $p < 0.001$). Although absolute biomass levels differed among products, the regional reconstruction reproduced several shared multi-decadal features, including lower biomass around the late 1980s to early 1990s and sustained increases after the mid-2000s.

These cross-product correlations were used as consistency checks rather than independent accuracy validation, because the products differ in training data, algorithms, and biomass ranges. The common-NFI comparisons in Section 3.2 therefore provide the primary evidence for quantitative performance differences.

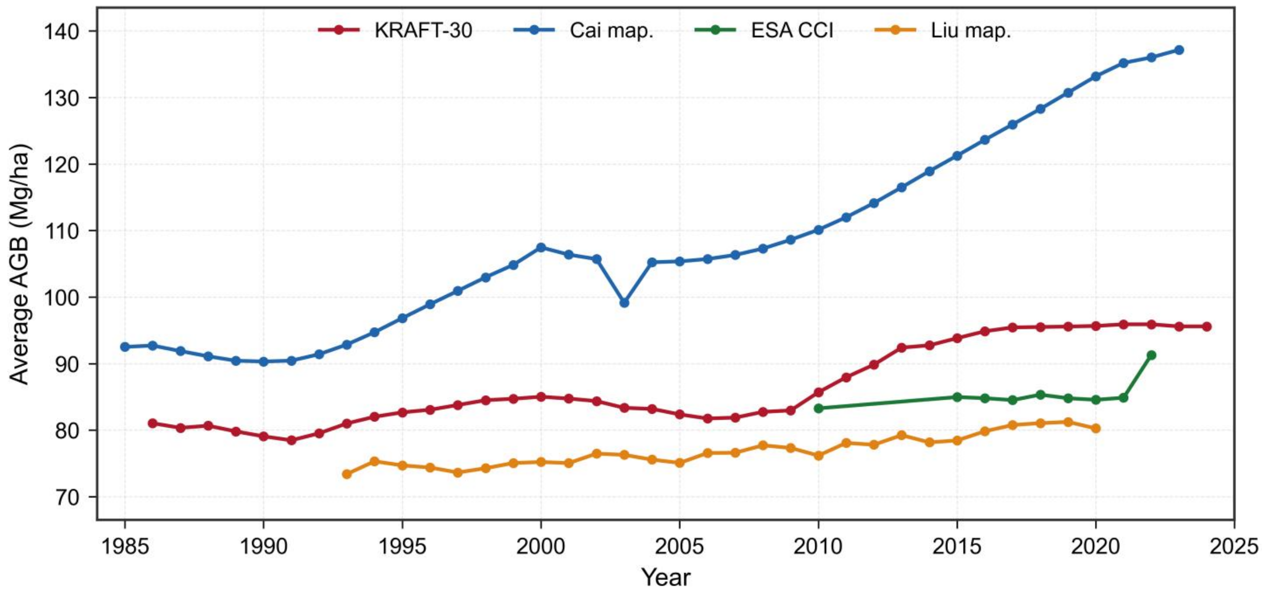

Figure 14. Temporal consistency comparison of annual mean forest AGB between KRAFT-30 and existing long-term forest AGB products in the study area.

Table 2. Temporal correlations between KRAFT-30 and existing annual forest AGB products based on annual mean forest AGB over overlapping years.

Comparison Products	Overlapping Years	Pearson r	Significance
Cai et al. AGB	1986-2023	0.96	$p < 0.001$
Liu et al. AGB	1993-2020	0.87	$p < 0.001$
ESA CCI AGB	2010, 2015-2022	_	_

Independent vegetation indicators provided a complementary temporal test (Fig. 15). Correlations between annual mean AGB and VOD, GPP, NPP, LAI, and SIF were 0.921, 0.632, 0.626, 0.943, and 0.939, respectively, over their periods of overlap. The coherent trajectories across canopy structure, productivity, greenness, and photosynthetic activity support the ecological plausibility of the reconstructed multi-decadal AGB signal while not substituting for field-based validation.

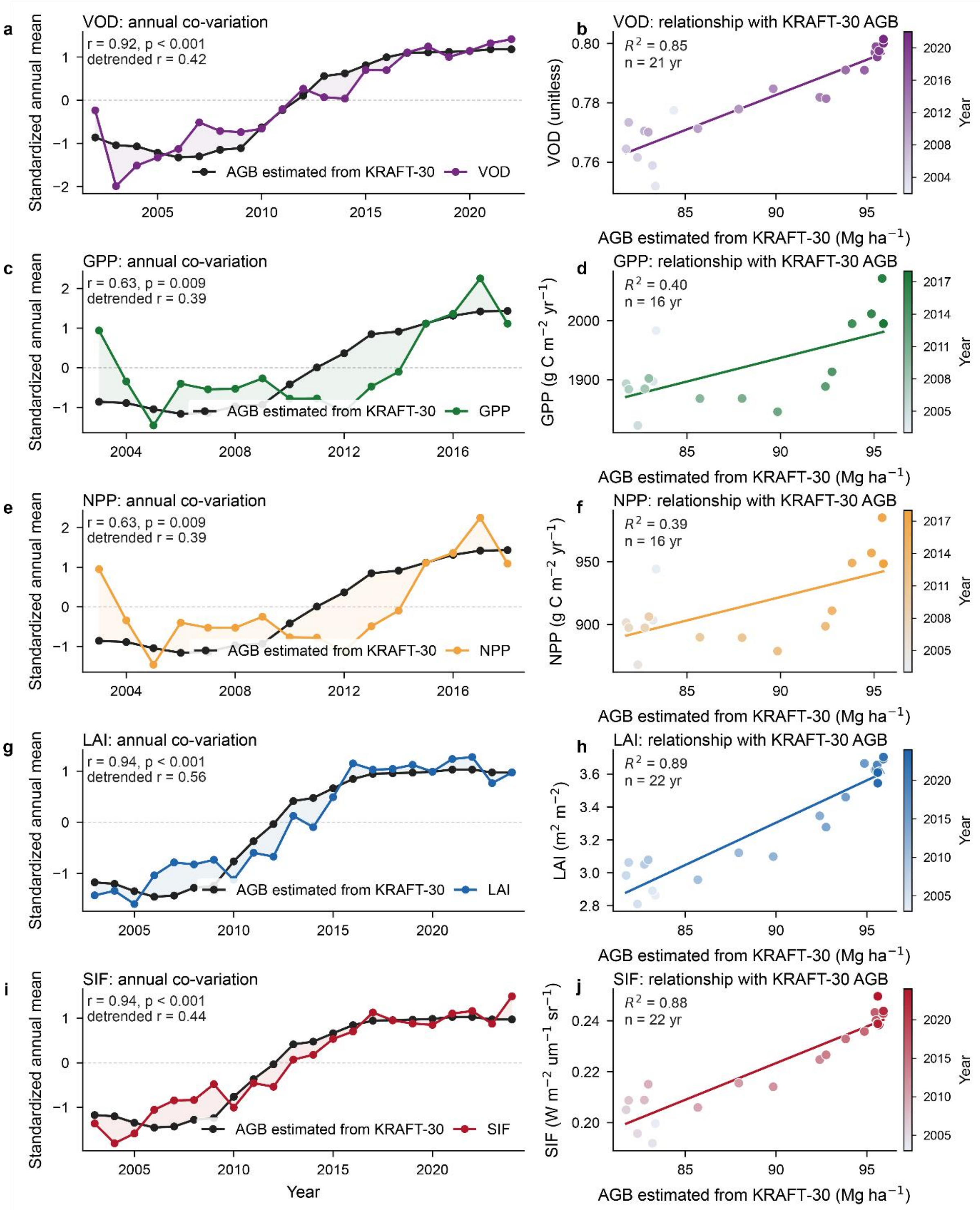

Figure 15. Temporal consistency between annual mean forest AGB and independent vegetation indicators. Left panels show annual co-variation with VOD, GPP, NPP, LAI, and SIF; right panels show the corresponding relationships over overlapping years.

3.4 Long-term forest biomass and aboveground-carbon dynamics

The annual reconstruction provides spatially continuous 30 m estimates of forest AGB across Southwest China's karst region for 1986–2024 (Fig. 16), enabling direct examination of long-term biomass patterns and spatial variability after the reconstruction framework had been independently evaluated.

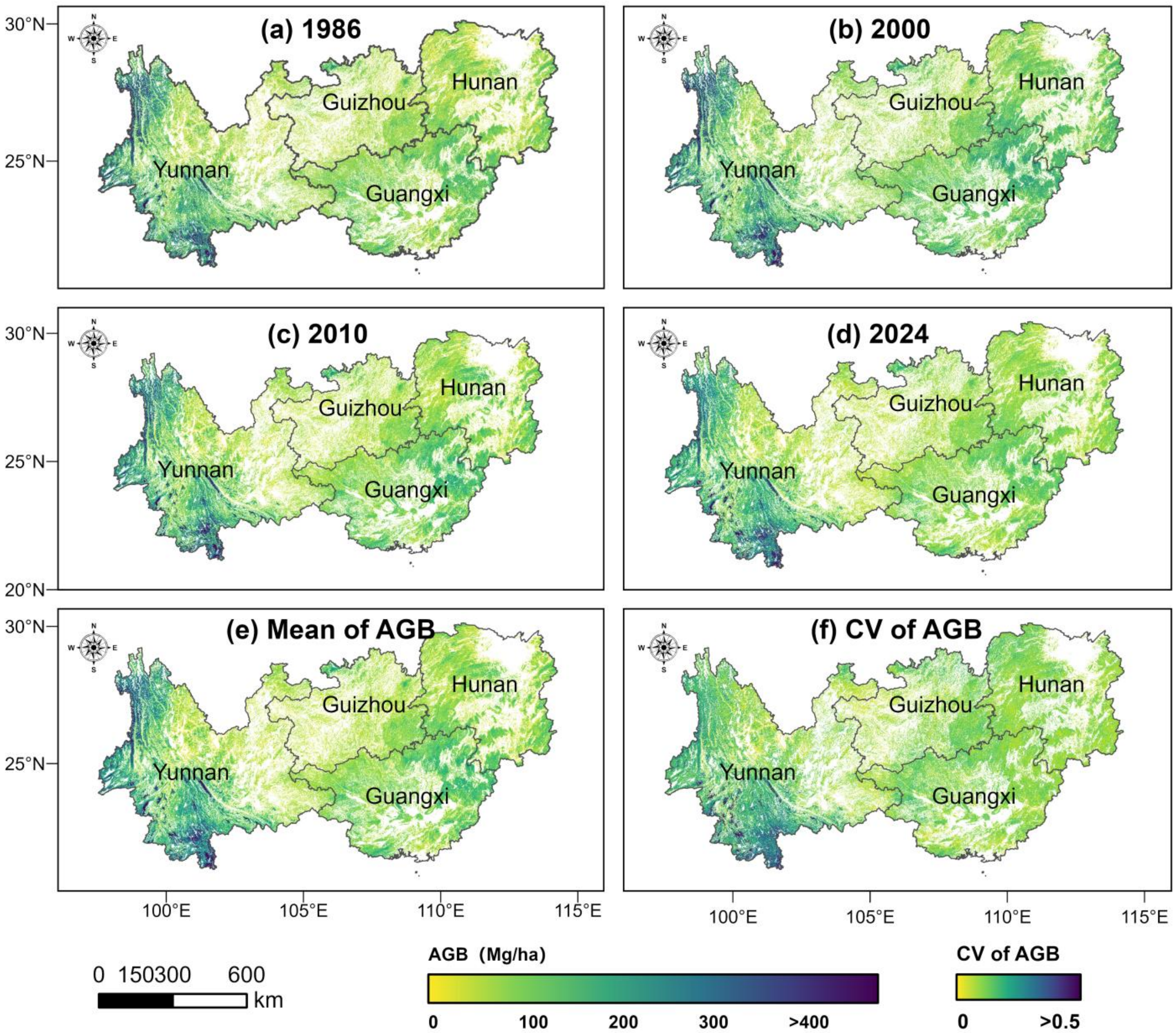

Figure 16. Spatial patterns and temporal variability of forest AGB in Southwest China's karst region from 1986 to 2024. (a)–(d) Spatial distributions of forest AGB in 1986, 2000, 2010, and 2024, respectively. (e) Spatial pattern of mean forest AGB during 1986–2024. (f) Temporal variability in forest AGB, expressed as the coefficient of variation, during 1986–2024.

Regional mean forest AGB increased significantly over 1986–2024, with clear interannual variability (Fig. 17b). Mean AGB rose from approximately 80 Mg ha^{-1} in 1986 to more than 100 Mg ha^{-1} during the 2010s. During the main growth phase from 1986 to 2018, the regional trend was approximately 0.48 Mg ha^{-1} yr^{-1} ($R^2 = 0.82$, $p < 0.001$). After 2019, the series showed a flatter trajectory and short-term fluctuations, reaching 95.60 Mg ha^{-1} in 2024.

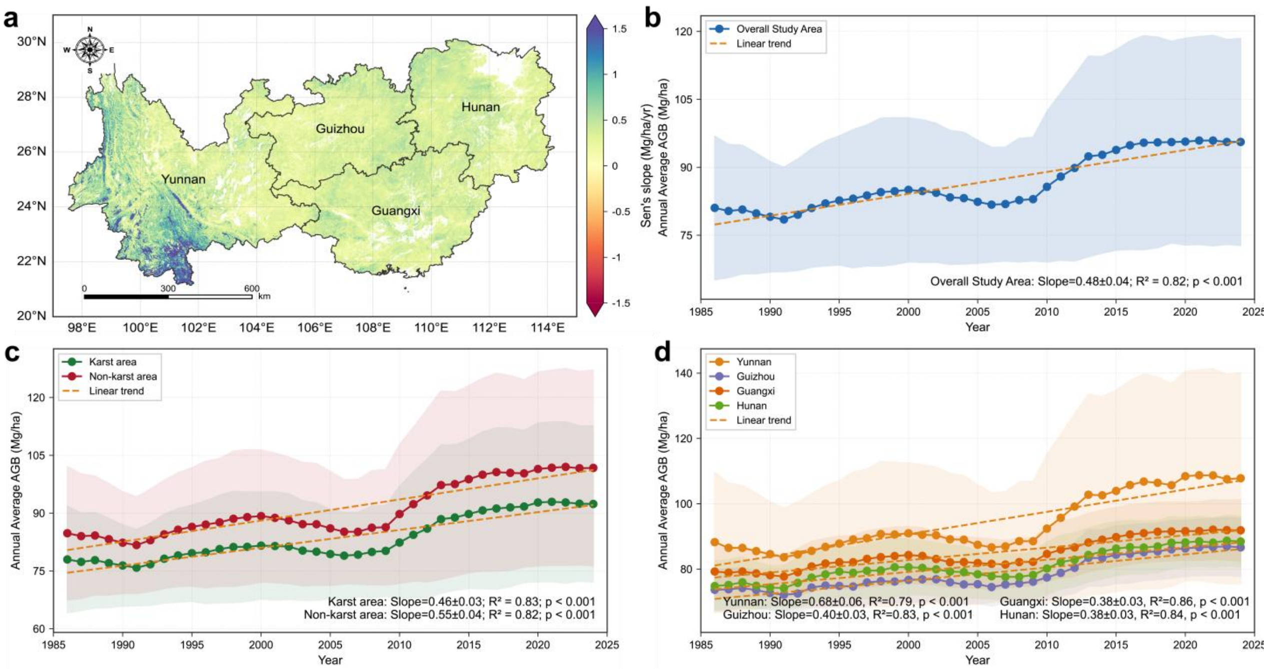

Figure 17. Forest AGB dynamics in Southwest China's karst region during 1986–2024.(a) Trend of forest AGB estimated using the Theil–Sen slope estimator. (b) Annual trajectory of regional mean forest AGB across the entire study area. (c) Annual mean forest AGB in karst and non-karst forest areas. (d) Annual mean forest AGB across Yunnan, Guizhou, Guangxi, and Hunan provinces.

Both karst and non-karst forests exhibited significant long-term biomass gains (Fig. 17c), with similar estimated rates of approximately 0.56 and 0.55 Mg ha^{-1} yr^{-1}, respectively. Provincial trajectories were more differentiated: Yunnan showed the largest increase (0.68 Mg ha^{-1} yr^{-1}), whereas Guizhou (0.40), Guangxi (0.38), and Hunan (0.38 Mg ha^{-1} yr^{-1}) increased more slowly but persistently (Fig. 17d).

Estimated aboveground forest carbon stock increased from approximately 2,200 Tg C in the late 1980s to nearly 2,800 Tg C in the late 2010s, corresponding to a long-term mean increase of 13.253 Tg C yr^{-1} (Fig. 18). Annual net changes nevertheless fluctuated substantially, including years with weak or negative change, illustrating that the annual reconstruction preserves short-term variability superimposed on the multi-decadal increase.

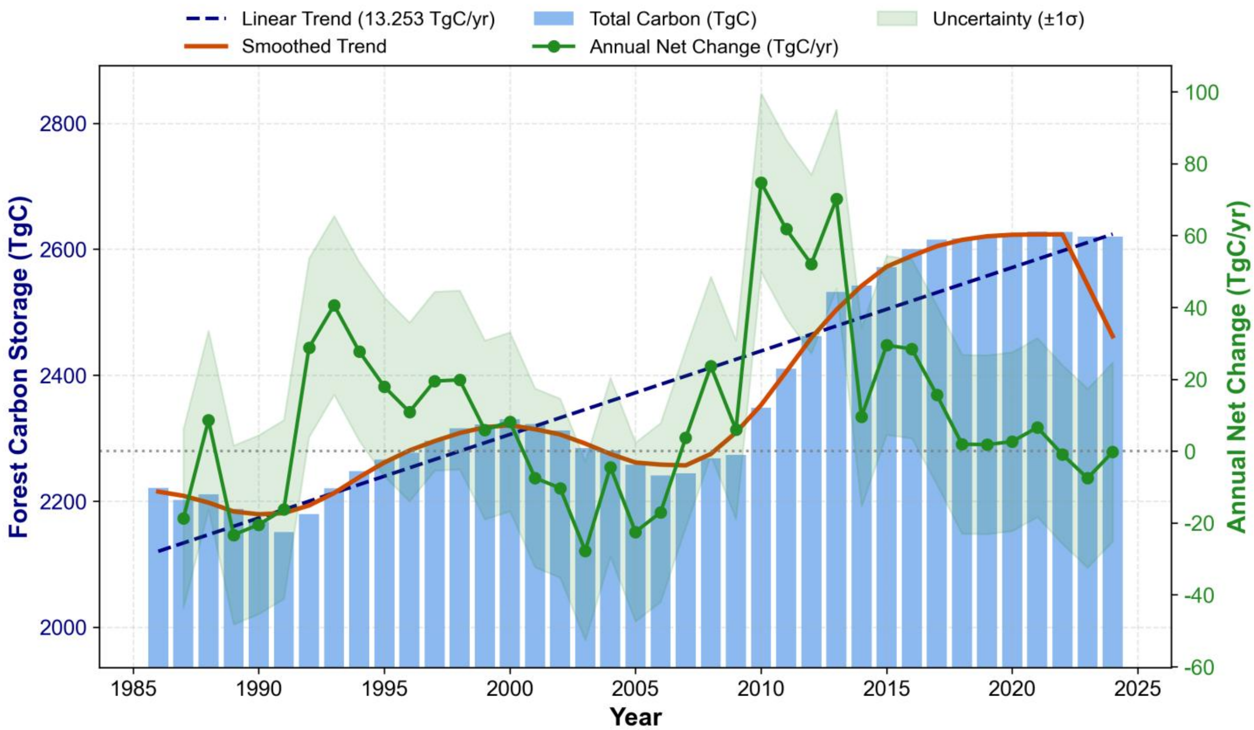

Figure 18. Long-term dynamics of forest carbon storage and carbon sink in Southwest China's karst region during 1986–2024.

4 Discussion

4.1 Regional adaptation and the two-stage reconstruction strategy

The central methodological contribution is the separation of regional spatial calibration from long-term temporal reconstruction. Instead of fitting sparse field plots directly to the full Landsat archive, the first stage uses contemporary NFI observations together with Sentinel-2, canopy height, terrain, and climate to establish a spatially detailed regional biomass baseline. The second stage transfers this regional biomass information to the Landsat record, which supplies the temporal continuity required for retrospective annual mapping. This design exploits complementary sensor strengths while keeping the historical model anchored to field-informed regional biomass structure.

Karst-specific adaptation enters at several points. NFI observations are drawn from the regional forest population; NDVI-weighted allocation improves spatial correspondence between plot support and 10 m imagery; canopy-height and terrain information help represent strong structural and topographic gradients; and biomass-stratified sampling prevents low-biomass pixels from dominating the Landsat training pool. These steps are particularly relevant in fragmented mountain forests, where mixed pixels, terrain effects, and uneven biomass distributions can degrade models calibrated for broader national domains.

The four-model comparison further shows that the framework does not depend on an assumed algorithmic choice. XGBoost was selected empirically because it produced the strongest test performance, while SHAP analysis confirmed that the final model remained primarily responsive to Landsat spectral information, with terrain providing secondary constraint. The resulting workflow is therefore best viewed as a regionally calibrated quantitative reconstruction strategy rather than a new machine-learning algorithm in itself.

This distinction is important for interpretation: the contribution lies in how multi-source regional calibration, biomass-balanced transfer, long-term Landsat observations, and independent comparison are combined to improve annual biomass reconstruction in a difficult landscape.

4.2 Quantifiable regional gains over existing AGB products

The strongest evidence for regional added value comes from direct validation and comparison under common references rather than from visual comparison alone. Across NFI-6–NFI-9, the regional reconstruction produced lower RMSE and MAE than the national annual AGB product in every inventory period, and its regional mean bias was less than half that of the national product (+16.6 versus +36.4 Mg ha^{-1}). Under the common NFI-9 comparison, it also showed the lowest overall error among the evaluated products. These comparisons directly address whether regional calibration yields measurable performance gains in Southwest China's karst forests.

The improvement is consistent with the structure of the calibration data. Regional NFI observations and canopy-height information expose the model to local biomass distributions and forest structural gradients that may be underrepresented in national or global training pools. The stratified transfer step further increases representation of scarce high-biomass conditions. This does not eliminate optical saturation, but the NFI residual analysis indicates weaker high-biomass underestimation than in the comparison products under the same field reference.

Spatial and structural comparisons provide complementary evidence. The 30 m reconstruction retains small patches, edge zones, and within-landscape gradients that are important in fragmented karst forests, while its relationship with airborne LiDAR CHM was stronger than that of the compared products. These gains should not be interpreted as universal superiority: large-area products remain valuable for national and global consistency. Rather, the results demonstrate that regional adaptation can materially improve local retrieval performance where landscape heterogeneity and training-domain mismatch are substantial.

4.3 Robustness of the multi-decadal annual reconstruction

Confidence in a 39-year annual reconstruction cannot be based on the 2019 model test set alone. The key temporal evidence is the four-cycle NFI evaluation, which provides field-based observations spanning 1999–2018 and shows stable correlations, lower error than the national annual product, and high directional agreement for adjacent-period changes. This independent temporal comparison is therefore more informative for historical reliability than the strong internal Landsat-model fit by itself.

Additional evidence comes from independent structural and ecological observations. Positive relationships with airborne LiDAR CHM and GEDI RH98 indicate that annual maps preserve plausible canopy-structure gradients, while strong co-variation with VOD, LAI, SIF, GPP, and NPP supports the regional temporal trajectory. Because these indicators are not direct AGB measurements, they are interpreted as corroborating evidence rather than substitutes for NFI validation.

The historical estimates are nevertheless anchored to a contemporary regional baseline, so baseline errors can propagate into earlier years and the forward three-year Landsat composite trades some year-specific sensitivity for improved observational continuity. Static terrain and environmental constraints may also preserve persistent regional gradients. These characteristics are intrinsic to retrospective reconstruction from sparse historical biomass observations and should be considered when interpreting abrupt pixel-level changes.

Importantly, the available independent tests indicate that this constraint did not prevent the reconstruction from reproducing multi-period NFI differences, broad structural gradients, or long-term vegetation trajectories. The product is therefore most defensible for regional annual monitoring, spatial comparisons, and multi-decadal trajectories rather than for attributing isolated single-pixel events without additional disturbance information.

4.4 Implications for long-term biomass recovery and carbon monitoring

The reconstructed series indicates a substantial long-term increase in forest AGB and aboveground carbon storage across Southwest China's karst region. The timing and direction of this increase are broadly consistent with previous evidence of forest recovery and densification in southern China (Tong et al., 2018, 2020, 2023), while the 30 m maps reveal strong spatial heterogeneity that is obscured in coarse regional averages.

Karst and non-karst forests both gained biomass, but provincial trajectories differed, with the largest long-term increase in Yunnan and slower gains in Guizhou, Guangxi, and Hunan. These contrasts provide spatially explicit observations for evaluating where biomass accumulation has been strongest and where forest carbon monitoring requires greater attention. Because the present study does not perform causal attribution, differences among geomorphological or administrative regions are interpreted as monitoring outcomes rather than evidence for specific climatic, edaphic, or management mechanisms.

This separation between observation and attribution is also useful for subsequent ecological studies: the annual reconstruction provides a validated biomass record that can be combined with climate, disturbance, forest age, or management information without embedding those drivers in the present retrieval analysis.

4.5 Limitations and transferability

Several limitations remain. Plot-to-pixel scale mismatch introduces unavoidable uncertainty into calibration and validation despite NDVI-weighted allocation and spatial matching. High-biomass forests also remain difficult for optical retrieval: residuals become increasingly negative above approximately 200–250 Mg ha^{-1}, consistent with spectral saturation and regression-to-the-mean effects. The estimates should therefore be interpreted more cautiously at the upper end of the biomass distribution.

Baseline uncertainty can propagate through the two-stage framework, and the forward moving-median compositing strategy smooths part of the year-to-year spectral variability in exchange for greater cloud-free continuity. The earliest Landsat years may contain fewer valid observations, while recent end-of-series composites have shorter forward windows. The semi-static forest mask also reduces classification noise but is not designed to represent every short-lived forest-cover transition.

External validation remains spatially and temporally incomplete: airborne CHM covers only part of the region, GEDI provides structural rather than direct AGB validation, and coarse vegetation indicators cannot replace field inventories. Additional repeated field plots, expanded airborne LiDAR, and more dynamic forest masks would further strengthen annual change evaluation. Application of the framework outside Southwest China would require regional recalibration and independent testing rather than assuming direct transferability.

5 Conclusions

This study demonstrates a regionally adapted two-stage strategy for reconstructing annual 30 m forest AGB in the heterogeneous karst landscapes of Southwest China from 1986 to 2024. A Sentinel-2/NFI baseline provided contemporary regional calibration, while biomass-stratified transfer to the Landsat archive enabled multi-decadal annual inference. The framework achieved strong baseline and reconstruction performance and, more importantly, produced measurable gains over existing products under common independent NFI comparisons, including lower error across four inventory cycles, reduced regional bias, and improved representation of biomass gradients and fine-scale forest structure. Multi-source structural and temporal checks further support the plausibility of the reconstructed trajectory. The annual series indicates sustained long-term biomass and aboveground-carbon accumulation with pronounced spatial and interannual variability. Taken together, the results show that regional calibration, balanced training-label transfer, and direct independent comparison can improve long-term quantitative biomass monitoring in complex forest landscapes while providing a consistent observational basis for subsequent carbon and restoration studies.

Declaration of competing interest

The authors declare that they have no known competing financial interests or personal relationships that could have appeared to influence the work reported in this paper.

Funding

This work was supported by the National Key Research and Development Program of China for Young Scientists [grant 2023YFF1305700], the Bagui Scholars Program of Guangxi, the National Natural Science Foundation of China [grant 42371129], and the Science and Technology Innovation Program of Hunan Province [grant 2024RC1067]. M.B. acknowledges funding from the European Research Council under the European Union’s Horizon 2020 Research and Innovation Programme [grant 947757, TOFDRY].

Data availability

The annual 30 m forest AGB maps generated in this study are publicly archived in Zenodo in three records because of repository storage limits: 1986–1998 (Yang, 2026a; https://doi.org/10.5281/zenodo.21371895), 1999–2011 (Yang, 2026b; https://doi.org/10.5281/zenodo.21425140), and 2012–2024 (Yang, 2026c; https://doi.org/10.5281/zenodo.21439480). Together, the three records contain the complete KRAFT-30 annual AGB raster series and metadata.

Pixel-level uncertainty layers were generated for the analyses reported here but are not included in the current Zenodo records because of repository storage limitations.

CRediT authorship contribution statement

Zezhi Yang: Conceptualization, Methodology, Software, Formal analysis, Investigation, Data curation, Visualization, Writing – original draft, Writing – review & editing. Xiaowei Tong: Conceptualization, Supervision, Fund, Project administration, Resources, Writing – review & editing. Xiaoxin Zhang: Writing – review & editing. Martin Brandt: Writing – review & editing. Fuming Xie: Visualization, Writing – review & editing. Yuemin Yue: Resources, Data curation. Kelin Wang: Resources, Data curation.

References

Breiman, L.: Random Forests, Mach. Learn., 45, 5–32, https://doi.org/10.1023/A:1010933404324, 2001.

Cai, Y., Zhu, P., Li, X., Liu, X., Chen, Y., Shen, Q., Xu, X., Zhang, H., Nie, S., Wang, C., Wang, J., Li, B., Wu, C., and Zhuang, H.: Dynamics of China's forest carbon storage: the first 30 m annual aboveground biomass mapping from 1985 to 2023, Earth Syst. Sci. Data, 17, 6993–7018, https://doi.org/10.5194/essd-17-6993-2025, 2025.

Chang, J., Tong, X., Brandt, M., Zhang, W., Yue, Y., Lu, J., Liu, S., Zhai, L., and Wang, K.: Tracking Southern China's Forest Growth from Space, J. Remote Sens., 5, 0810, https://doi.org/10.34133/remotesensing.0810, 2025.

Chen, D., Fan, L., Peng, J., Lannoy, G. D., Wigneron, J.-P., Frappart, F., Tao, S., Wang, M., Li, X., Liu, X., Wang, H., Yuan, Q., Chen, X., Xiao, Y., and Ciais, P.: A global long-term (2002–2022) C-band vegetation optical depth record retrieved after merging AMSR-E, AMSR2 and WindSat, Int. J. Appl. Earth Obs. Geoinformation, 145, 104961, https://doi.org/10.1016/j.jag.2025.104961, 2025.

Chen, T. and Guestrin, C.: XGBoost: A Scalable Tree Boosting System, Proceedings of the 22nd ACM SIGKDD International Conference on Knowledge Discovery and Data Mining, 785–794, https://doi.org/10.1145/2939672.2939785, 2016.

Drucker, H., Burges, C. J. C., Kaufman, L., Smola, A., and Vapnik, V.: Support Vector Regression Machines, Advances in Neural Information Processing Systems 9, 155–161, 1997.

Drusch, M., Del Bello, U., Carlier, S., Colin, O., Fernandez, V., Gascon, F., Hoersch, B., Isola, C., Laberinti, P., Martimort, P., Meygret, A., Spoto, F., Sy, O., Marchese, F., and Bargellini, P.: Sentinel-2: ESA's optical high-resolution mission for GMES operational services, Remote Sens. Environ., 120, 25–36, https://doi.org/10.1016/j.rse.2011.11.026, 2012.

Dubayah, R., Blair, J. B., Goetz, S., Fatoyinbo, L., and Hansen, M.: The Global Ecosystem Dynamics Investigation: High-resolution laser ranging of the Earth's forests and topography, Sci. Remote Sens., 1, 100002, https://doi.org/10.1016/j.srs.2020.100002, 2020.

Earth Science Data Systems, N.: GEDI L2A Elevation and Height Metrics Data Global Footprint Level V002 | NASA Earthdata, 2025.

Efroymson, M. A.: Multiple regression analysis, in: Mathematical Methods for Digital Computers, edited by: Ralston, A. and Wilf, H. S., John Wiley & Sons, New York, 191–203, 1960.

Farr, T. G., Rosen, P. A., Caro, E., Crippen, R., Duren, R., Hensley, S., Kobrick, M., Paller, M., Rodriguez, E., Roth, L., Seal, D., Shaffer, S., Shimada, J., Umland, J., Werner, M., Oskin, M., Burbank, D., and Alsdorf, D.: The Shuttle Radar Topography Mission, Rev. Geophys., 45, 2005RG000183, https://doi.org/10.1029/2005RG000183, 2007.

Fick, S. E. and Hijmans, R. J.: WorldClim 2: new 1-km spatial resolution climate surfaces for global land areas, Int. J. Climatol., 37, 4302–4315, https://doi.org/10.1002/joc.5086, 2017.

He, Y., Shu, S., Holm, J., Needham, J., Negron-Juarez, R., Koven, C., Zhu, Q., and Falco, N.: Forest aboveground biomass estimation through integration of sentinel-2 and PALSAR-2 time series: assessing models trained on GEDI and field inventory benchmarks, ISPRS J. Photogramm. Remote Sens., 236, 668–689, https://doi.org/10.1016/j.isprsjprs.2026.04.022, 2026.

Hijmans, R. J., Cameron, S. E., Parra, J. L., Jones, P. G., and Jarvis, A.: Very high resolution interpolated climate surfaces for global land areas, Int. J. Climatol., 25, 1965–1978, https://doi.org/10.1002/joc.1276, 2005.

Jiang, Z., Lian, Y., and Qin, X.: Rocky desertification in Southwest China: Impacts, causes, and restoration, Earth-Sci. Rev., 132, 1–12, https://doi.org/10.1016/j.earscirev.2014.01.005, 2014.

Ku, H. H.: Notes on the Use of Propagation of Error Formulas, J. Res. Natl. Bur. Stand. Sect. C Eng. Instrum., 70C, 263–273, https://doi.org/10.6028/JRES.070C.025, 1966.

Lang, N., Jetz, W., Schindler, K., and Wegner, J. D.: A high-resolution canopy height model of the Earth, Nat. Ecol. Evol., 7, 1778–1789, https://doi.org/10.1038/s41559-023-02206-6, 2023.

Le Toan, T., Quegan, S., Davidson, M. W. J., Balzter, H., and Paillou, P.: The BIOMASS mission: Mapping global forest biomass to better understand the terrestrial carbon cycle, Remote Sens. Environ., 115, 2850–2860, https://doi.org/10.1016/j.rse.2011.03.020, 2011.

Li, X. and Xiao, J.: A Global, 0.05-Degree Product of Solar-Induced Chlorophyll Fluorescence Derived from OCO-2, MODIS, and Reanalysis Data, Remote Sens., 11, 517, https://doi.org/10.3390/rs11050517, 2019.

Liu, G., Ciais, P., Tao, S., Yang, H., Xiao, C., and Bastos, A.: A Moderate-Resolution, Long-Term Global Radar-Based Forest Above-Ground Biomass Dataset from 1993 to 2020, https://doi.org/10.5281/zenodo.19259660, n.d.

Liu, J., Li, S., Ouyang, Z., Tam, C., and Chen, X.: Ecological and socioeconomic effects of China's policies for ecosystem services, Proc. Natl. Acad. Sci. U. S. A., 105, 9477–9482, https://doi.org/10.1073/pnas.0706436105, 2008.

Lu, D., Chen, Q., Wang, G., Liu, L., Li, G., and Moran, E.: A survey of remote sensing-based aboveground biomass estimation methods in forest ecosystems, Int. J. Digit. Earth, 9, 63–105, https://doi.org/10.1080/17538947.2014.990526, 2016.

Lu, F., Hu, H., Sun, W., Zhu, J., and Liu, G.: Effects of national ecological restoration projects on carbon sequestration in China from 2001 to 2010, Proc. Natl. Acad. Sci. U. S. A., 115, 4039–4044, https://doi.org/10.1073/pnas.1700294115, 2018.

Lundberg, S. M. and Lee, S.-I.: A Unified Approach to Interpreting Model Predictions, Advances in Neural Information Processing Systems 30, 4765–4774, https://doi.org/10.5555/3295222.3295230, 2017.

Ma, L., Liu, Y., Zhang, X., Ye, Y., Yin, G., and Johnson, B. A.: Deep learning in remote sensing applications: A meta-analysis and review, ISPRS J. Photogramm. Remote Sens., 152, 166–177, https://doi.org/10.1016/j.isprsjprs.2019.04.015, 2019.

Masek, J. G., Vermote, E. F., Saleous, N. E., Wolfe, R., Hall, F. G., Huemmrich, K. F., Gao, F., Kutler, J., and Lim, T.-K.: A Landsat surface reflectance dataset for North America, 1990–2000, IEEE Geosci. Remote Sens. Lett., 3, 68–72, https://doi.org/10.1109/LGRS.2005.857030, 2006.

McKay, M. D., Beckman, R. J., and Conover, W. J.: A Comparison of Three Methods for Selecting Values of Input Variables in the Analysis of Output from a Computer Code, Technometrics, 21, 239–245, https://doi.org/10.1080/00401706.1979.10489755, 1979.

Mitchard, E. T. A.: The tropical forest carbon cycle and climate change, Nature, 559, 527–534, https://doi.org/10.1038/s41586-018-0300-2, 2018.

Pan, Y., Birdsey, R. A., Fang, J., Houghton, R., and Kauppi, P. E.: A large and persistent carbon sink in the world's forests, Science, 333, 988–993, https://doi.org/10.1126/science.1201609, 2011.

Puliti, S., Breidenbach, J., Schumacher, J., Hauglin, M., Klingenberg, T. F., and Astrup, R.: Above-ground biomass change estimation using national forest inventory data with Sentinel-2 and Landsat, Remote Sens. Environ., 265, 112644, https://doi.org/10.1016/j.rse.2021.112644, 2021.

Roy, D. P., Kovalskyy, V., Zhang, H. K., Vermote, E. F., Yan, L., Kumar, S. S., and Egorov, A.: Characterization of Landsat-7 to Landsat-8 reflective wavelength and normalized difference vegetation index continuity, Remote Sens. Environ., 185, 57–70, https://doi.org/10.1016/j.rse.2015.12.024, 2016.

Santoro, M. and Cartus, O.: ESA Biomass Climate Change Initiative (Biomass_cci): Global datasets of forest above-ground biomass for the years 2007, 2010, 2015, 2016, 2017, 2018, 2019, 2020, 2021 and 2022, v6.0, https://doi.org/10.5285/95913ffb6467447ca72c4e9d8cf30501, 2025.

Santoro, M., Cartus, O., Carvalhais, N., Rozendaal, D. M. A., Avitabile, V., Araza, A., de Bruin, S., Herold, M., Quegan, S., Rodríguez-Veiga, P., Balzter, H., Carreiras, J., Schepaschenko, D., Korets, M., Shimada, M., Itoh, T., Moreno Martínez, Á., Cavlovic, J., Cazzolla Gatti, R., da Conceição Bispo, P., Dewnath, N., Labrière, N., Liang, J., Lindsell, J., Mitchard, E. T. A., Morel, A., Pacheco Pascagaza, A. M., Ryan, C. M., Slik, F., Vaglio Laurin, G., Verbeeck, H., Wijaya, A., and Willcock, S.: The global forest above-ground biomass pool for 2010 estimated from high-resolution satellite observations, Earth Syst. Sci. Data, 13, 3927–3950, https://doi.org/10.5194/essd-13-3927-2021, 2021.

Sen, P. K.: Estimates of the Regression Coefficient Based on Kendall's Tau, J. Am. Stat. Assoc., 63, 1379–1389, https://doi.org/10.1080/01621459.1968.10480934, 1968.

Sibanda, M., Mutanga, O., and Rouget, M.: Examining the potential of Sentinel-2 MSI spectral resolution in quantifying above ground biomass across different fertilizer treatments, ISPRS J. Photogramm. Remote Sens., 110, 55–65, https://doi.org/10.1016/j.isprsjprs.2015.10.005, 2015.

Su, Y., Shi, T., Zhang, X., Xu, Y., Cheng, K., Liu, S., Han, G., Ma, X., Chen, S., Tong, X., Li, W., Gong, W., Guo, Q., Brandt, M., Piao, S., d'Aspremont, A., and Ciais, P.: Substantial contribution of trees outside forests to above-ground carbon across China, Commun. Earth Environ., 7, 131, https://doi.org/10.1038/s43247-025-03150-y, 2026.

Tong, X., Brandt, M., Yue, Y., Horion, S., and Wang, K.: Increased vegetation growth and carbon stock in China karst via ecological engineering, Nat. Sustain., 1, 44–50, https://doi.org/10.1038/s41893-017-0004-x, 2018.

Tong, X., Brandt, M., Yue, Y., Ciais, P., and Jepsen, M. R.: Forest management in southern China generates short term extensive carbon sequestration, Nat. Commun., 11, 129, https://doi.org/10.1038/s41467-019-13798-8, 2020.

Tong, X., Brandt, M., Yue, Y., Zhang, X., Fensholt, R., Ciais, P., Wang, K., Liu, S., Zhang, W., Mao, C., and Jepsen, M. R.: Reforestation policies around 2000 in southern China led to forest densification and expansion in the 2010s, Commun. Earth Environ., 4, 260, https://doi.org/10.1038/s43247-023-00923-1, 2023.

Vermote, E., Justice, C., Claverie, M., and Franch, B.: Preliminary analysis of the performance of the Landsat 8/OLI land surface reflectance product, Remote Sens. Environ., 185, 46–56, https://doi.org/10.1016/j.rse.2016.04.008, 2016.

Wang, K., Zhang, C., Chen, H., Yue, Y., Zhang, W., Zhang, M., Qi, X., and Fu, Z.: Karst landscapes of China: patterns, ecosystem processes and services, Landsc. Ecol., 34, 2743–2763, https://doi.org/10.1007/s10980-019-00912-w, 2019.

Wang, X., Zhong, B., Chang, B., Zhang, Y., Li, S., Du, B., Qiao, Y., Cai, H., Wu, J., Yang, A., Jian, Y., Su, J., Wang, G., and Liu, Q.: A 30 m aboveground biomass dataset for multiple vegetation types in China (2020), Sci. Data, 12, 1777, https://doi.org/10.1038/s41597-025-06053-x, 2025.

Wulder, M. A., Loveland, T. R., Roy, D. P., Crawford, C. J., and Masek, J. G.: Current status of Landsat program, science, and applications, Remote Sens. Environ., 225, 127–147, https://doi.org/10.1016/j.rse.2019.02.015, 2019.

Xiao, Z., Liang, S., Wang, J., Xiang, Y., Zhao, X., and Song, J.: Long-Time-Series Global Land Surface Satellite Leaf Area Index Product Derived From MODIS and AVHRR Surface Reflectance, IEEE Trans. Geosci. Remote Sens., 54, 5301–5318, https://doi.org/10.1109/TGRS.2016.2560522, 2016.

Yang, J. and Huang, X.: The 30 m annual land cover dataset and its dynamics in China from 1990 to 2019, Earth Syst. Sci. Data, 13, 3907–3925, https://doi.org/10.5194/essd-13-3907-2021, 2021.

Yang, Q., Niu, C., Liu, X., Feng, Y., Ma, Q., Wang, X., Tang, H., and Guo, Q.: Mapping high-resolution forest aboveground biomass of China using multisource remote sensing data, GIScience Remote Sens., 60, 2203303, https://doi.org/10.1080/15481603.2023.2203303, 2023.

Yang, Z.: KRAFT-30: An annual 30 m forest above-ground biomass dataset for Southwest China's karst region from 1986 to 2024, Part 1: 1986–1998, https://doi.org/10.5281/zenodo.21371895, 2026a.

Yang, Z.: KRAFT-30: An annual 30 m forest above-ground biomass dataset for Southwest China's karst region from 1986 to 2024, Part 2: 1999–2011, https://doi.org/10.5281/zenodo.21425140, 2026b.

Yang, Z.: KRAFT-30: An annual 30 m forest above-ground biomass dataset for Southwest China's karst region from 1986 to 2024, Part 3: 2012–2024, https://doi.org/10.5281/zenodo.21439480, 2026c.

Yuan, W., Liu, S., Yu, G., Bonnefond, J.-M., Chen, J., Davis, K., Desai, A. R., Goldstein, A. H., Gianelle, D., Rossi, F., Suyker, A. E., and Verma, S. B.: Global estimates of evapotranspiration and gross primary production based on MODIS and global meteorology data, Remote Sens. Environ., 114, 1416–1431, https://doi.org/10.1016/j.rse.2010.01.022, 2010.

Zeng, W., Tomppo, E., Healey, S. P., and Gadow, K. V.: The national forest inventory in China: history, results, international context, For. Ecosyst., 2, 23, https://doi.org/10.1186/s40663-015-0047-2, 2015.

Zheng, Y., Shen, R., Wang, Y., Li, X., Liu, S., Liang, S., Chen, J. M., Ju, W., Zhang, L., and Yuan, W.: Improved estimate of global gross primary production for reproducing its long-term variation, 1982–2017, Earth Syst. Sci. Data, 12, 2725–2746, https://doi.org/10.5194/essd-12-2725-2020, 2020.